

Isomer Studies in the $f_{7/2}$ shell

MASTER OF SCIENCE THESIS

Pedro Montuenga

Supervisor: Prof. Dr. Dirk Rudolph



LUND
UNIVERSITY

DEPARTMENT OF PHYSICS
NUCLEAR STRUCTURE GROUP
LUND UNIVERSITY
2007

Contents

1	Introduction	5
2	Theoretical Background	9
2.1	The Nuclear Shell Model	9
2.2	Mirror Nuclei	12
2.3	Electromagnetic Properties	12
2.4	The Spin of Isomeric States in the ^{43}V Experiment	12
3	Description of the Experiment	15
3.1	Objectives of the experiment	15
3.2	Experimental setup	15
3.3	The FRagment Separator	16
3.3.1	Components of the FRS	16
3.3.2	The Wedge Degradar	17
3.3.3	Particle Identification	18
3.3.4	Stopper and implantation	20
3.3.5	Ge-Detectors	21
3.4	Conditions for the ^{43}V experiment	21
3.4.1	Computer simulations in LISE++	21
3.4.2	Layout optimization	22
4	Isotope Identification Using the FRS Detectors	25
4.1	Calibration Settings	25
4.2	Raw Data	26
4.3	Basic Particle Identification	26
4.3.1	Time of Flight in Scintillators	27
4.3.2	MUSIC Position Correction	28
4.3.3	Proton Number Z	29
4.3.4	Signal in the MUSIC Detectors	29
4.3.5	Mass-to-charge ratio A/Q	32
4.4	Comparison of the Ti Positions	32
4.5	Development of Track1 and Track2	36
5	Isomer Study	39
5.1	Isotope-Gated γ Analysis	39
5.2	^{43}Ti analysis	40

5.2.1	Long Time Range Analysis	40
5.2.2	Medium Time Range Analysis	45
5.3	^{38}K	48
5.4	^{45}Cr	48
5.5	Half Life Calculation	49
5.5.1	^{43}Ti Isomeric Analysis	53
5.5.2	^{38}K Isomeric Analysis	62
5.5.3	^{45}Cr Isomeric Analysis	62
6	Analysis and Conclusions	67
6.1	Data Acquisition and Isotope Differentiation	67
6.2	Isomeric Analysis	68
6.2.1	^{43}Ti	68
6.2.2	^{38}K	71
6.2.3	^{45}Cr	73
7	Popularvetenskaplig Sammanfattning	77
8	Acknowledgments	79

Chapter 1

Introduction

Nuclear physics is one of the fields in physics that has both evolved and collaborated the most to modern day science from the beginning of the twentieth century. It has been a never ending source of applications in various fields such as medical and environmental technologies, astrophysics, energy generation, and material sciences. Since the existence of the atomic nucleus was proposed by Ernest Rutherford in 1911, science is determined to probe the underlying principles that rule the behaviour of the particles comprising the atomic nucleus.

However, current nuclear models based on quantum mechanics are far from being a holistic description of the behaviour of nuclear matter. Nuclear experiments are fundamental to prove –or disprove– and enhance our theoretical description of the laws that govern the comportment of the nucleus and its components.

One important physical phenomenon that occurs in the atomic nuclei is the presence of isomeric states. **Nuclear isomers** are metastable states of the nuclei for which the radioactive properties are different to those of the ground state and live for a certain period of time. But although unstable, some isomers can live up to millions of years, while most isomers live to the order of nano- or microseconds. The longest living known isomeric state is the 9^- state in ^{180}Ta . This isomer has a half-life of more than $1.5 \cdot 10^{15}$ years and occurs in Nature. Another important isomeric state is the 16^+ in ^{178}Hf , which has a half life of about 31 years

Several nuclear isomers have been found practical applications. The $1/2^-$ states in ^{95}Tc and ^{99}Tc , for example, are used in medical and industrial applications. Isomers can also help to understand the manner in which the nuclear forces in the nucleus work. Studying the properties of isomeric states can be used to corroborate the current nuclear models.

The “Rare Isotope Investigation” (RISING) campaign at GSI seeks to study the nature of excited states in nuclei. This campaign studies short-lived radioactive nuclei through isomer spectroscopy. These radioactive nuclei are produced by means of relativistic projectile fragmentation within energies in the range 500 - 1000 MeV/u. In order to produce such conditions the SIS synchrotron at GSI is used. This beam of

accelerated particles impinges on a ^9Be target to generate exotic nuclei in states with energies above the ground state energy. The products of this reaction are afterwards accelerated and separated to be identified in the FRS. After the FRS, a final focal plane contains 15 high-efficiency germanium detectors in order to take fingerprints of the decay process of the ions. For more information on the FRS and the experimental assembly refer to Chapter 3 of this thesis.

The process that makes possible the creation of exotic nuclei is called projectile fragmentation. Projectile fragmentation occurs when a heavy projectile collides against a light target nucleus with high enough energies as to overcome the Coulomb repulsion, leading to a strong interaction between the nuclei. In Figure 1 a simplified scheme of a projectile fragmentation is shown.

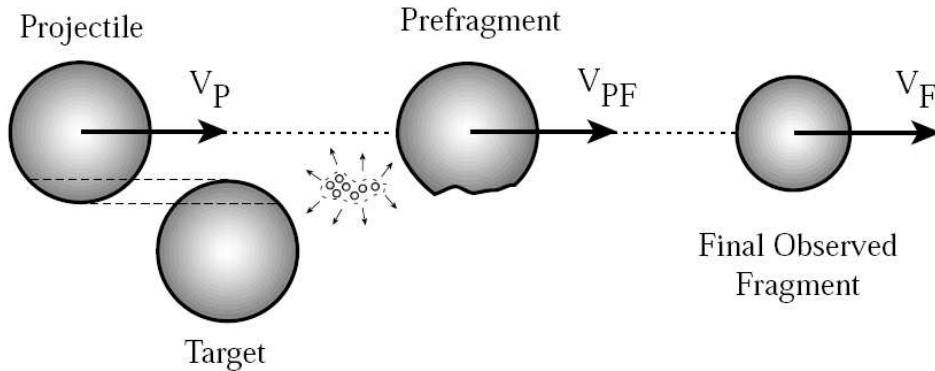


Figure 1.1: A simplistic picture of the projectile fragmentation process. A fraction of the projectile interacts beyond the Coulomb potential with the target (abrasion) and is cut out. The remaining fraction of the incoming projectile remains unchanged during the impact and afterwards evaporates particles and γ -decays until reaching a ground state or an isomeric state. The image was taken from [1].

The projectile fragmentation process can be divided in two parts [2]: the abrasion, in which the contact between the two happens and the overlapping regions of the nuclei, also known as the “participants” in the reaction are cut off. The abrasion phase lasts roughly 10^{-21}s . The second step of the projectile fragmentation is called the ablation process and during it the remnant of the fragment –the so-called “spectator”– remains almost intact and goes through a depletion phase for about 10^{-16}s . During the undergoing of the ablation, the nucleus evaporates particles and γ -decays until reaching the ground state or, until being trapped in an isomeric state.

With this abrupt reaction mechanism, together with high energy and different impact parameters, seemingly any isotope on the nuclidic chart can be produced. However, the most likely reaction products of fragmentation reactions follow the line of beta-stability. Therefore, if a stable beam is fragmented, the production cross sec-

tion for drip-line nuclei is low.

This thesis comprises data from the stopped beam campaign within RISING. Our work consists of an experimental study of possible isomers in nuclei in the vicinity of ^{43}V . These experiments were performed during March 2006.

In the next chapter the most important theoretical definitions will be explained. In Chapter 3 the experiment in itself, as well as how the conditions to optimize it, is described. Chapter 4 illustrates how the delineation of each isotope was performed, while the isomeric studies are depicted in Chapter 5. Chapter 6 seeks to examine and make conclusions about the experimental results and the data analysis.

Chapter 2

Theoretical Background

An atomic nucleus is made up by two particles: the protons and the neutrons. Nucleon is a generic term used to refer both to neutrons and protons. To describe the behaviour of nuclear matter, two main forces of nature have to be considered: the strong force and the electromagnetic force. While the strong force interaction between nucleons is attractive and independent of the nature of the nucleon (whether if it is a proton or a neutron), the electromagnetic force in the nucleus acts as a repulsive force between the protons. If the Coulomb repulsion in a nucleus exceeds the strong force attraction the nucleus is dismantled. Even necessary though this chapter is not intended to be a detailed source of all the theoretical concepts handled in this thesis, an overview of all notions is necessary.

2.1 The Nuclear Shell Model

Nucleons are spin 1/2- particles and must therefore obey the Pauli principle. It is known that the two-neutron separation energies show discontinuities at certain neutron numbers like 2, 8, 20, 28, 50, 82, and 126. These are known as *magic numbers*. In order to describe the motion of nucleons what one has to do is to solve the Schrödinger equation with the Hamiltonian for an \mathcal{N} -particle system,

$$\mathcal{H} = \sum_{i=1}^{\mathcal{N}} \left(-\frac{\hbar^2}{2m} \nabla_i^2 \right) + \frac{1}{2} \sum_{i \neq j}^{\mathcal{N}} v(\vec{r}_i, \vec{r}_j). \quad (2.1)$$

The first term of this equation characterizes the kinetic energy of the nucleons. The right term characterizes the interaction between the nucleons given by a potential that is a function of the position of every single one of them.

The solution of a system like this is a wave function that is the product of the single-particle wave functions. Since the number of nucleons in a nucleus tends to be always above 2 or 3, it is compulsory to make approximations to the interaction between nucleons in order to obtain an appropriate approximation of the system. One example of a good approximation is an average potential. This average potential is chosen so that any residual interaction is minimized. A typically resorted average

potential is the central potential. This potential allows us to write the potential as two separate potentials where one of them is central and the other is angular. In this case the angular potential is independent of the central and can be solved by the introduction of the quantum number l . This atomic number is related to the orbital angular momentum \vec{l} as $\vec{l}^2 |\psi\rangle = l(l+1)\hbar^2 |\psi\rangle$, where $|\psi\rangle$ is the single-particle wave function.

The l quantum-number can only take integer values and is denoted as s, p, d, f, g , etc; corresponding to $l = 1, 2, 3, 4, 5$, etc. The orbital angular momentum can have different projections with respect to a given quantum axis, let us call z . This projection is given by $l_z |\psi\rangle = m_l \hbar |\psi\rangle$, where m_l can take values $l, l-1, \dots, 0, \dots, -l+1, -l$.

An analogous definition to the quantum number l is the intrinsic spin of the nucleons, \vec{s} , and the projection on z can be defined as $s_z |\psi\rangle = m_s \hbar |\psi\rangle$, where $m_s = \pm 1/2$.

The parity π , is an indicative of the symmetry of the wave function with respect to the spatial coordinates. States with even l are symmetric, and have thus a parity of 1; and states with odd l are antisymmetric and have a parity of -1.

One central potential that that reflects the matter-density distribution of the nucleus is the Woods-Saxon potential, shown in Figure 2.1(a):

$$V_{\text{WS}}(r) = \frac{-V_0}{1 + \exp(\frac{r-R}{a})}; \quad (2.2)$$

With V_0 being the depth, R the nuclear radius, and a a parameter. The problem with this Hamiltonian is that the gaps between the eigenvalues gaps do not correspond to those seen experimentally after 20. This potential is then enhanced by the introduction of a spin-orbit interaction potential, which manages to reproduce these magic numbers as seen in Figure 2.1(b). For a more thorough description on the spherical shell model, see [3, 4]. The potential then becomes:

$$V(r) = \frac{-V_0}{1 + \exp(\frac{r-R}{a})} + V_{\text{SO}} \vec{l} \cdot \vec{s}. \quad (2.3)$$

The Second term of the potential couples the orbital angular momentum \vec{l} to the intrinsic spin \vec{s} to form an angular momentum \vec{j} . The same way \vec{l} and \vec{s} have quantum numbers l and s , \vec{j} has its related quantum number j and its projection on a given axis $m_j = m_l + m_s$. This spin-orbit interaction splits the degeneracy of each $l > 0$ level into two, $j = l \pm 1/2$ so that the level $j = l + 1/2$ is lowered in energy. With the energy scheme of our potential we can predict the energy of the ground state of spherical nuclei. The first thing is to treat protons and neutrons separately. The total parity of a nucleus is the product of the parities of the single-particle wave functions. For all even-even nuclei, i.e., nuclei for which both the number of protons and neutrons are even, the spin and parity of the ground state are $J^\pi = 0^+$. For odd-even nuclei the spin and parity are given by the odd particle. For odd-odd nuclei the last odd proton and neutron contribute to the spin. Therefore we must couple these two spins, j_n and j_p . So that:

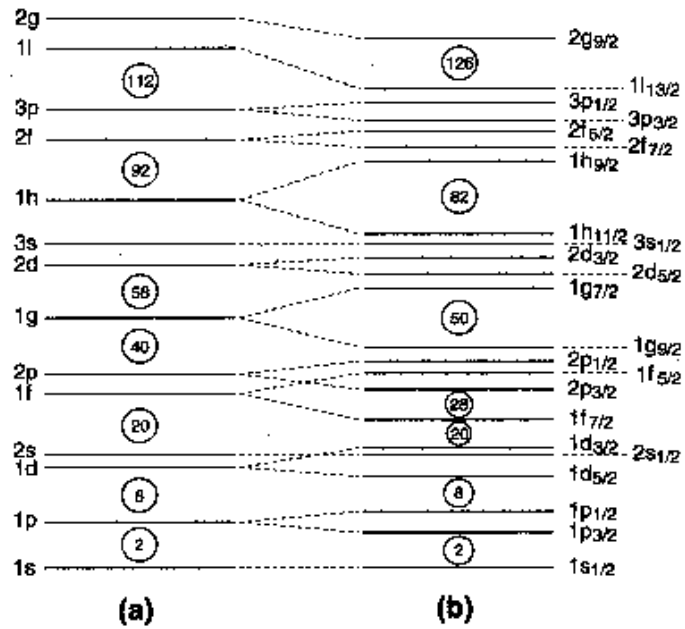


Figure 2.1: Comparison of the eigenenergies for the Woods-Saxon potential. In (a) the energy levels come from a WS potential without spin orbit interaction. In (b) the WS potential is added a spin-orbit coupling. Numbers in circles are the magic numbers. Scheme taken from [5].

$$|j_p - j_n| \leq J \leq |j_p + j_n|. \quad (2.4)$$

With these rules we can predict the ground state spin and parity but only to a certain extent. In ^{51}Mn , for instance, the predicted ground state according to the theory would be $7/2^-$, but experimentally it is found to be $5/2^-$. Discrepancies like this could be explained by saying that maybe not all nuclei are spherical in their ground state.

2.2 Mirror Nuclei

As was said before, the strong force is the same for protons and neutrons. Actually we can consider protons and neutrons as the same particle but with opposite isospin projection with, let us say, protons having an isospin projection of $t_z = -1/2$ for the proton and for the neutron of $t_z = +1/2$. The Coulomb repulsion, however, breaks the isospin symmetry. Mirror nuclei are nuclei with the same mass for which the number of protons in one is the number of neutrons in the other one. One example of two mirror nuclei is the pair $^{54}_{28}\text{Ni}_{26}$ and $^{54}_{26}\text{Fe}_{28}$. Knowing, for example the energy scheme for a nucleus it is possible to predict what the energy scheme would be like for its mirror nucleus.

2.3 Electromagnetic Properties

A quantum theory of radiation can be done through analogy to the classical one. We can introduce multipole operators $\mathcal{M}(\sigma L)$. These operators describe the change of a nucleus between two different states. This radiation field σ can be of an electric or magnetic nature. The multipole order L carries an angular momentum of $L\hbar$ per photon, such as $L = 1$ represents a dipole transition, $L = 2$ a quadrupole, etc. For a more profound approach to the electromagnetic properties of the nuclei refer to [6, 7, 8]. The character of the radiation is determined by the change of parity and the change of polarity. The parity selection rules for the character of the multipole transition are

$$\begin{aligned} \pi_i \neq \pi_f \quad L \text{ odd} &\rightarrow \text{electric, } L \text{ even} \rightarrow \text{magnetic,} \\ \pi_i = \pi_f \quad L \text{ even} &\rightarrow \text{electric, } L \text{ odd} \rightarrow \text{magnetic.} \end{aligned} \quad (2.5)$$

2.4 The Spin of Isomeric States in the ^{43}V Experiment

The aim of this work is to make a map of the energy level scheme for several isotopes around ^{43}V in the nuclidic chart. We desire to obtain these isotopes with excited states of spin ≤ 10 . As a rule of thumb, the more nucleons that are removed from the projectile, the higher the spin that can be produced. At the same time the production cross section decreases the further away the projectile is from the fragment of interest. We are using ^{58}Ni nuclei, and we will be working with nuclei with masses around $A = 37$ and $A = 48$. Taking away 10 nucleons or more from our beam particles is

more than enough in order to populate the isomers.

In order to argue that the loss of 10 or more nucleons is sufficient as to populate isomeric states of $I \leq 10$ we refer to [9]. In this experiment a $19/2^-$ isomer was produced in ^{43}Sc by fragmentation of ^{46}Ti . This was done with a big enough population. Therefore, it is logical to think that the loss of 10 or more nucleons will populate isomeric states of values as high as $I = 10$.

Chapter 3

Description of the Experiment

3.1 Objectives of the experiment

The experiment of our interest was carried out during March 2006 at GSI. Our focus will be the analysis of the data regarding ^{43}V . Using **projectile fragmentation** of a ^{58}Ni beam as our experimental method, we are able to produce and study exotic nuclei in addition to the known isotopes ^{43}Ti and ^{43}Sc , which have isomeric $19/2^-$ states. The experimental settings of the FRS and associated detector systems had to be optimized for this region of the nuclidic chart. Our overall aim was to search for previously unknown isomeric states in nuclei around ^{43}V and determine their lifetimes. For a more detailed explanation on how these conditions were optimized I refer to Section 3.4.

3.2 Experimental setup

The experimental setup used in the RISING Stopped-Beam Campaign is located at the Gesellschaft für Schwerionenforschung, GSI, situated at the outskirts of Darmstadt in Germany. Our primary beam is made of ^{58}Ni and is accelerated in the SIS synchrotron, which is able to speed up ions with magnetic rigidities up to $B\rho = 18\text{ Tm}$. This limit is equivalent to energies between 1.0 and 4.5 GeV per atomic mass unit, using atoms from H to U. The **Magnetic Rigidity** is a measure of magnetic bending resilience and depends on ionic charge, mass and translational energy –less charge, higher mass and higher kinetic energy yields a higher magnetic rigidity and vice versa–. Our beam then impinges on a target of ^9Be at the entrance of the FRagment Separator. The FRS is a magnetic forward device that handles relativistic ions and the functioning of which is explained in the following.

3.3 The FRagment Separator

The FRS is a magnetic forward spectrometer. It comprises four parts, and each of them includes a 30° dipole magnet and an ensemble of quadrupoles, before and after the dipole, to achieve first-order focusing conditions. It can be switched to either achromatic –for having well separated, narrow distributions of positions of ions– or monochromatic mode, if one prefers a narrow momentum distribution at the focal plane. A Scheme of the FRS can be seen in Figure 3.1. This graphic was taken from [10].

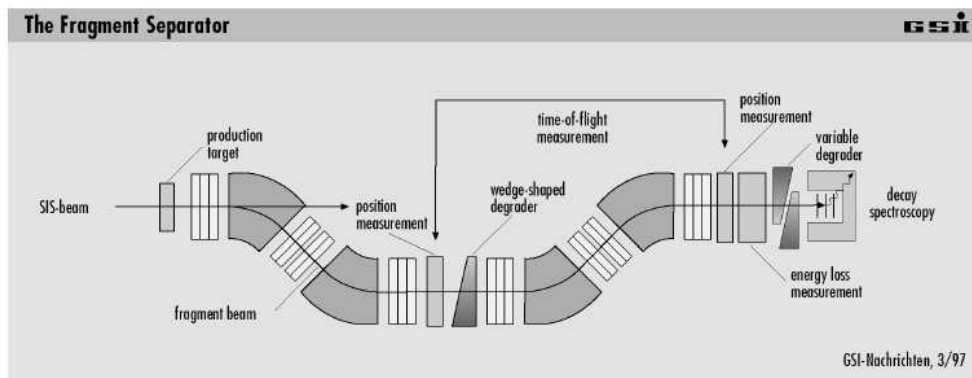


Figure 3.1: Outlook of the FRS sections at the GSI facility

The ion-optical system can be corrected for second-order aberrations using sextupole magnets. Since the required sextupole fields are small, aberrations of third and higher order are minimized. According to calculations more than 90 % of the first-order momentum resolution is restored for a beam with 20π mm mrad of transverse emittance and a momentum spread of $\Delta p = 2\%$.

3.3.1 Components of the FRS

The elements that are comprised in the FRS are listed next in the same order as the beam passes through them:

- **Target Area:** After leaving the SIS Synchrotron by penetrating its vacuum window, the beam hits one of the production targets, mounted on a ladder, that remotely can be moved into the beamline.
- **S1 Area:** Passing through the first ion optical section, the beam reaches the first focal plane. Here, the frequently used “S1 slit” is located.
- **S2 Area:** At the second focal plane reside the so-called “Sc21 Scintillator”, the S2 slit, and a wedge shaped energy degrader. Additional components like stripper foils of detectors optionally can be mounted on a ladder located behind the wedge.

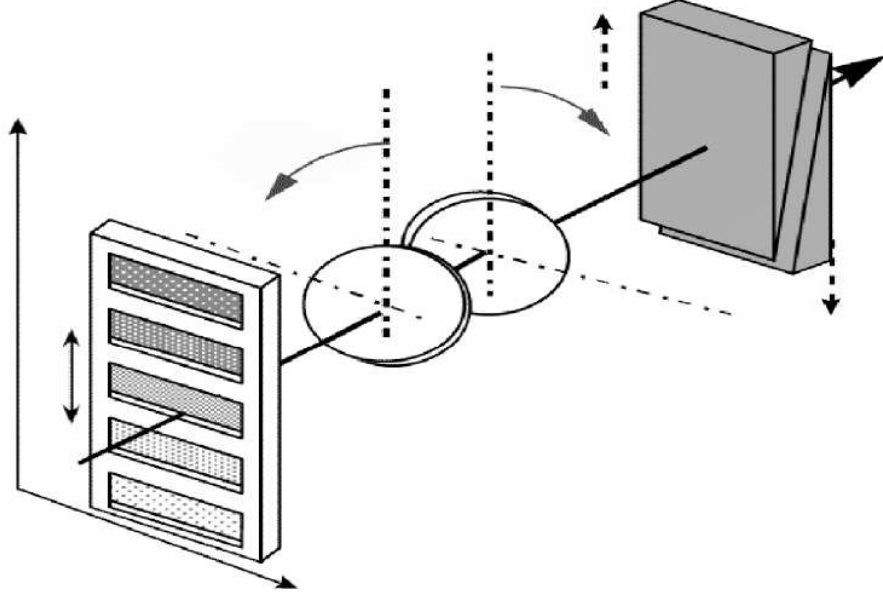


Figure 3.2: This figure shows the three elements of the Wedge-shaped energy degrader. These yield a fully tunable degrader. Illustration from [12]

- **S3 Area:** The third focal plane resembles the S1 area. Usually it is not used for more than its “S3 slit”.
- **S4 Area:** At the end of the FRS, the final focal plane is used for an experiment’s detector set-up and for particle identification with the detectors described in Section 3.3.3. The S4 components are sitting in air, which does not make much of a difference at the relativistic ion energies, but yet the amount of air has to be considered for proper implantation of the ions in a stopper.

All FRS components like slits, ladders, and degraders are remotely tunable and all components in the beamline can be removed in that manner.

3.3.2 The Wedge Degrader

The wedge-shaped energy degrader has the important task of separating the incoming ions as a function of their charge, according to the Bethe-Bloch formalism in Equation 3.1, which approximates the energy loss per distance traveled [11]:

$$-\frac{dE}{dx} = \frac{4\pi}{m_e c^2} \cdot \frac{nZ^2}{\beta^2} \left(\frac{e^2}{4\pi\epsilon_0} \right)^2 \cdot \left[\ln \frac{2m_e c^2 \beta^2}{I \cdot (1 - \beta^2)} - \beta^2 \right], \quad (3.1)$$

where n is the electron density of the target, $\beta = v/c$, and I is the mean excitation potential of the target.

It is important to consider that the separation produced in the wedge is not spatial. In order to make a spatial separation of the ions, the second half of the FRS plays a fundamental role. This spatial separation is based on the magnetic rigidities of the ions.

The energy degrader also allows us to make momentum distributions of the ions more narrow in achromatic mode. A thicker degrader would give us momentum distributions with smaller widths.

The wedge shaped energy degrader is composed of three parts which are (See Figure 3.2) :

1. **Disk:** It consists of two different, thick inclined disks that can be rotated against each other to create a range of angles.
2. **Wedge:** The two wedges can be shifted vertically in order to generate different thicknesses. The thickness ranges from 1 to 25 mm and is a function of the x position in S2 because of the angle between them.
3. **Ladder:** Composed of five different plates ranking from 16 mm to 80 mm of aluminium, in 16 mm steps. This ladder is used when a very thick degrader is required.

3.3.3 Particle Identification

One of the most –if not the most– essential parts of FRS experiments is the correct in-flight identification of the nuclear reaction products. In order to accomplish this, a set of detectors is used, most of them mounted on a special table in the S4 area, after the final ion optical section of the FRS, and prior to its final focal plane (see Figure 3.3). The measurables that are used for correct identification are the ion positions at the fourth and final focal plane, the scintillator times and energies at the intermediate and final focal plane, and the energy loss of the ions in two ionization chambers in the S4 area.

Scintillators

The **Scintillation Detectors** are made of firm plastic and are placed at the second and fourth focal planes of the FRS. Scintillator Sc21 at the second focal plane installed for our experiment is a 3.39 mm plastic scintillator. Sc21 and Sc41 are read out from four sides to give both the x and y -position of a passing ion. Sc42, however, is read out from left and right only, and the veto Sc43 is read only from one side.

Even though scintillators do not provide a very high resolution for calculating the **energy loss**, this function can come in handy in order to discriminate products from secondary reactions. This energy loss is estimated through the product of the signals coming from the four or two sides of the detector.

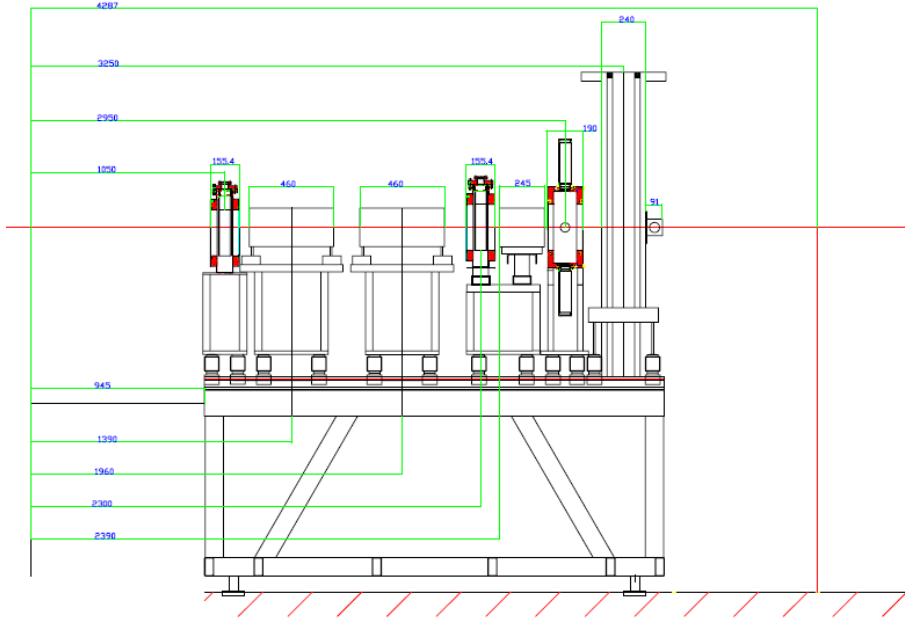


Figure 3.3: Technical overview of the S4 table and its detectors. All distances are measured with respect to the exit of the final quadrupole magnet. Moving from the final quadrupole magnet downstream, i.e. toward increasing distances in the drawing, the different components are: MW41, MUSIC41, MUSIC42, MW42, S4 slit, Sc41, Degrader, Sc42. The use of the detectors is described in the text

The **position** can be retrieved with the time difference between the two signals. A defocused primary beam is used to illuminate the Sc detectors and two MWs at the same time. The fitting of the tracked x -position dependence on the time difference produces a second or higher-order polynomial.

In order to measure the **time-of-flight**, the 1 mm thick Sc41 gives the start signal and the delayed signal from Sc21 marks the stop of the measurement. This way of measuring the time of flight ensures that events do not swamp the data stream. The general rule for this time difference measurement is to start the clock with the detector counting least. Sc42 is placed behind the wedge-shaped degrader to measure if the ions survived the slowing-down process. The 5 mm thick Sc43 detects ions that were not implanted in the stopper. The time of flight is normally determined by averaging the time difference between the scintillators Sc21 and Sc41.

Multi Wire detectors

The **multiwire**, “MW detectors” in the FRS setup are used for the measurement of the x - and y -positions of passing ions that contribute to the total resulting flux from the original beam. The detector comprises a gas chamber filled with a CO₂-argon

mixture and three thin wire grids. The electrons from ionizations in the detector gas, which are caused by passing ions, are collected by an anode grid. This is how we can measure the positions. Their typical resolution is about 0.5 mm and they cover an area of 20×20 cm. Each MW transmits one anode time and four cathode times. Times can be linked to position of the interaction in the detector

MW detectors are assembled in pockets at S1, S2, and S3 for possible use there. These detectors have 100 μm thick titanium vacuum windows to screen the FRS vacuum. Two MW can be mounted on the S4 table, MW41 and MW42. Situated in air, 25 μm thick kapton windows are used instead of titanium windows. For choosing the appropriate events, the x and y cathode times have to be independent of trigger timing, the anode times are then subtracted [13]. In order to determine the position, the relative positions on both axes on the i th detector only considers the legitimate events. Using the properties of the MW delays and potential offsets the absolute positions are calculated. With two (or more) detectors provided we can track the trajectory of each particle. In order to extrapolate the trajectory of a given particle we calculate first the angle considering the distance between two MW and a focus.

MUSIC detectors

The **MULTIPLE SAMPLING IONIZATION CHAMBER, MUSIC**, outputs a signal that is proportional to the amount of ionization caused by a passing ion. The detector gas is composed of 90% of argon and 10% of methane. The ions and electrons produced in the ionizations drift towards the cathode and segmented anodes, respectively. The produced charge is proportional to the square of the passing ions' charges and inversely proportional to the kinetic energy, and thus gives a measure of nuclear charge if the ion is fully stripped. For this reason, two MUSICs are set up at S4 in this experimental campaign. Ions are likely to change their charge state when not fully striped, while passing through the layers of matter between the MUSICs. This helps the correct identification of heavy ions' nuclear charge Z .

To obtain corrected positions we fit the dependence of the energy measured by the MUSIC –obtained by illuminating the MUSIC detector and calibrated position-sensitive detectors simultaneously– on the x position –determined with MW tracking. This correction is done with a second or higher-order polynomial¹.

3.3.4 Stopper and implantation

At the final focal plane of the FRS, the beam can be stopped with a so-called catcher or stopper. Ions with too low energy will be stopped in layers of matter prior to the stopper, e.g., Sc42, while ions with too high energies will pass right through it. Ions passing through the stopper are to be detected by Sc43, which is used as a veto detector. Making use of MOCADI and LISE++ simulations and the veto detector, one can ensure that the ions are properly implanted. Experimentally one can make sure that this does not happen through the S4 degrader. The stopper is located in the center of the array of germanium detectors.

¹analogously to the calibration of the time difference into absolute position in the scintillation detectors.

3.3.5 Ge-Detectors

A set of 15 EUROBALL cluster detectors in closed formation is ensembled around the final focal plane of the FRS. Each of the clusters has seven individual germanium crystals, adding up to a total of 105 crystals. Each crystal has its own set of electronics and the array has an overall 1 MeV peak efficiency in excess of 15%. Figure 3.4 shows a picture of the Ge-detector array.

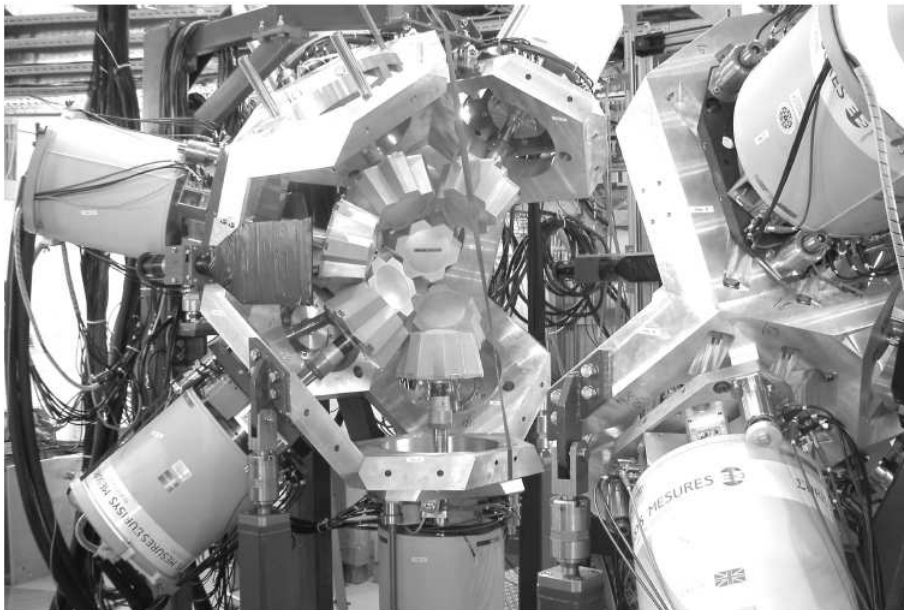


Figure 3.4: The opened Ge-detector array still missing one Euroball cluster at the upper left. Note the Swedish cluster in the lower left of the picture[10].

3.4 Conditions for the ^{43}V experiment

3.4.1 Computer simulations in LISE++

LISE++ is a software developed in order to simulate the transmission and yields of fragments produced and collected in a spectrometer. Using a very friendly environment that allows to include in the simulated experiment every single feature of the original one, LISE++ becomes a very useful tool for obtaining expedite results of the experiment. Unlike other software like MOCADI, that can make more precise estimates of the outcome and that are more frequently resorted to when doing the most rigorous calculations, LISE++ is normally used to obtain an estimate of how certain alterations to the experiment would change the aftermath of it. MOCADI simulations are resorted to in our analysis (see Section 4.4) . LISE++ is also capable of optimizing the values of some quantities in order to collect large statistics for the experiment.

When downloaded, LISE++ has already files of different spectrometers. The FRS is also part of these. This file only features the basic components, but more components can be added and changed without much trouble. Detectors and other layers of additional matter are to be included. Different sorts of building blocks can be chosen from. LISE++ produces different plots coming from the different elements of the experiment that can be compared to the actual ones from the real experiment. It is important to mention that in LISE++ the x positions are inverted with respect to our measurements in the plane of scintillator SC21. So this means that from now on when comparing the experiment's results and the LISE++ predictions, the positions in the x axis in the S2 plane of LISE++ will be inverted.

3.4.2 Layout optimization

The experimental ^{43}V setting was optimized to perform a scanning type of experiment, i.e. to study many different nuclei at the same time. In order to accomplish this, the required criteria for optimization can be summarized as:

- The isotopes ^{45}Cr , ^{44}V , and ^{40}Sc should be inside the scanned area.
- A large number of additional isotopes should reach the final focal plane of the FRS, with ion distribution widths that allow for easy particle identification.
- The 'setting fragment' should be chosen in a way that gives a neither too high, nor too low S2 and S4 rate, and yet permit the study of proton-drip-line nuclei with reasonable statistics.

The first variables of the experiment that had to be taken into consideration were:

- The target: A thin target has the advantage of giving only little additional spread and ensures small momentum distribution widths. It also reduces the effective production rate through a lower production yield. A thick target, on the other hand, gives additional position spread and broader distributions, but serves as well as an energy degrader and provides a higher yield. Let us remember that the objective was to allow several elements' momenta to be within the FRS acceptance.
- The wedge: A thin wedge would be convenient if one wants to permit a large area of the nuclidic chart to be covered.
- The S4 degrader: Covering a wide area of the nuclidic chart, the S4 should be thick enough in order to decelerate the ions coming from a thin target and a thin wedge.

One has to consider as well that such a thin target would require thicknesses that were not available for the energy degrader. It was decided that having a higher production was more important than having more narrow momentum distributions. This is the reason why the thickest target was chosen in the end.

With these conditions $24 N \leq Z$ nuclei from $\text{K}(Z = 19)$ to $\text{Mn}(Z = 25)$ were transmitted reasonably well. Although the thickest target was used, the degrader

also had to be massive. The chosen one in particular was 4200 mg/cm^2 . Because of the large range of proton number of the ions, a thicker or denser stopper than the actual $4\text{ mm } ^9\text{Be}$ plate, which was used for the main ^{54}Ni setting [10], is needed. Simulations in MOCADI and LISE++ suggest that a 12 mm plastic stopper would stop all ions except for very light ones. We show next a table where all the settings for the ^{43}V are shown with their actual values:

Table 3.1: Settings for the ^{43}V experiment

Setting Unit	S1 B_ρ [Tm]	Wedge [mg/cm ²]	Wedge Angle [mrad]	S3 B_ρ [Tm]	S4 Degrader [mg/cm ²]
^{43}V Prod.	6.1781	2000	2.8847	5.5154	4200

In the LISE++ simulations a Z vs A/Q plot can be obtained. Figure 3.5 shows an example of how this plot would look like.

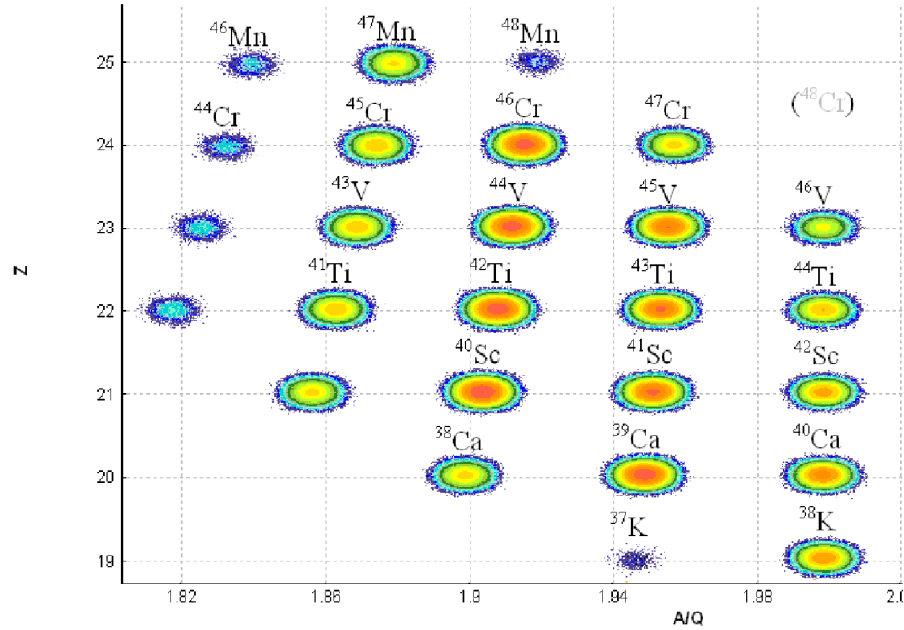


Figure 3.5: A LISE++ simulation of the Z vs A/Q plot. The 24 isotopes of our interest are highlighted

Chapter 4

Isotope Identification Using the FRS Detectors

This chapter explains the general method for identifying the different isotopes with the detectors placed in S2 and S4 in order to convert the raw data into actual physical quantities. The first thing to do then, is to show how the results looked like before the analysis. Next it illustrates how the particle identification was performed based on the calculation of Z and A/Q . Thirdly, it compares the positions of four isotopes of a prolific element in our experiment such as Ti to LISE++ and MOCADI predictions at both S2 and S4. Finally, this chapter intends to explain the motivation for considering the tracking without the MW's in order to obtain higher statistics.

4.1 Calibration Settings

In order to do the calibration, a low intensity primary beam was used. This beam has to be centered throughout the FRS. The different settings used to do the calibration were [10, 13]:

1. **Primary beam, no target or detectors:** Only vacuum windows and thin particle detectors like the Multiwire detectors.
2. **Primary beam, Sc21 in:** Scintillation detector 21 is inserted into the beam-line.
3. **Primary beam, target and Sc21:** The ^9Be target is added. The beam is recentered.
4. **Four Wedge Settings:** The wedge shaped energy degrader is put in. Four settings are created with four different wedge thicknesses.

The main parameters obtained from this calibration are shown in Table 4.1.

Table 4.1: Calibration Settings – predicted setting parameters.

Setting No. Unit	S1 $B\rho$ [Tm]	Wedge [mg/cm ²]	S3 $B\rho$ [Tm]	MUSIC41 ΔE [MeV]	S2-S4 T_{flight} [ns]
1	7.9478	0	7.9478	—	—
2	7.9478	0	7.7878	—	—
3	7.6724	0	7.5553	—	—
4.1	7.6724	4500	6.1970	326.6	179.9
4.2	7.6724	5300	5.9118	341.0	184.5
4.3	7.6724	5800	5.7230	351.8	187.8
4.4	7.6724	6500	5.4425	370.0	193.2

4.2 Raw Data

The data, consisting of the so-called events, puzzled together by the electronics and software of the experimental setup. Files containing the event information help us to extract it to produce histogram files and plots. Although a categorization of the events had to be done in order to search for all the information that is not evident at first sight, contemplating the raw data can give some information. In order to show an example of how the data looked originally we take a glance at the ΔE vs T_{flight} plot, which is represented in figure 4.1. ΔE is the energy loss measured in the MUSIC41 detector that is strongly related to Z . T_{flight} is the time of flight between the two scintillator detectors and is associated to A/Q .

Here we can see several counts in various points. We can also see how it is cut out both on the left and on the right because of the FRS acceptance. Outside from 90 and 200 in the horizontal axis there are no counts whatsoever. We also appreciate that even if we consider some of these diffuse “blobs” to be a certain isotope, there are several counts in between for which it would be hard to tell which ion they belonged to. Nevertheless, even with these raw signals it seems possible to select a given isotope rather easily for there is a fairly sufficient separation between the different Z s. For this analysis, 24 isotopes will be studied. In Figure 4.1 all of the identified isotopes are highlighted.

It was logical to think that the energy loss is bigger for elements with a higher charge (remember the Bethe-Bloch formula in Equation 3.1). We can thus say that the upper elements are the ones with a higher charge. On the other hand, as a consequence of their mass, the heavier elements will travel more slowly and will have bigger times-of-flight.

4.3 Basic Particle Identification

We are to explain now how the mass-to-charge ratio and the proton number are computed through the time-of-flight between the two scintillators, the energy loss in the MUSIC detectors amongst other quantities measured. Before we show how the

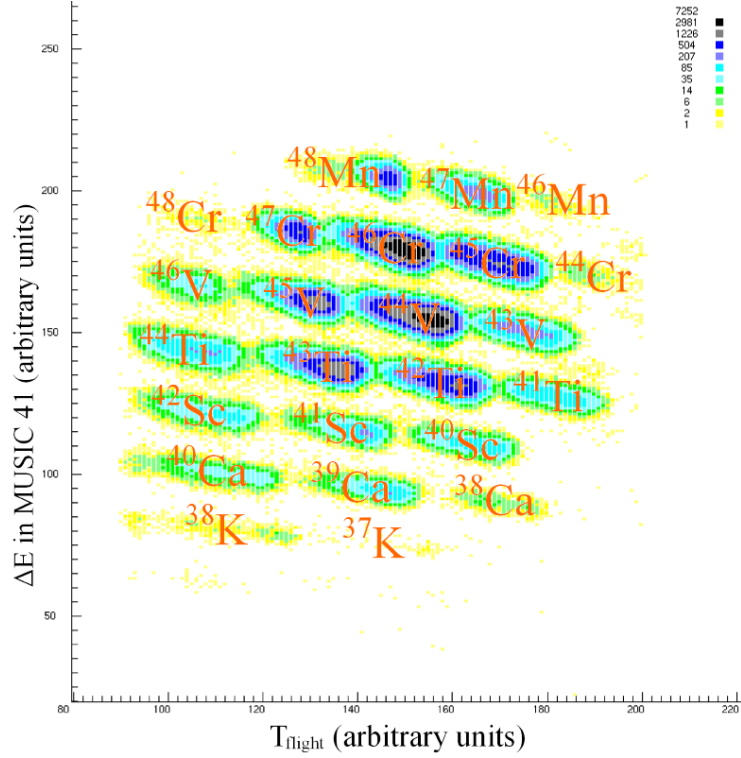


Figure 4.1: Raw ΔE signal for MUSIC41 vs the time-of-flight measured between Sc21 and Sc41 on the x axis plot. The total number of events here is around 6.4 million. Arbitrary units are used in both axes. The 24 isotopes analyzed in this experiment are distinguished. Note that since the timer on Sc21 was delayed and was used to mark the stop in the measurement, the time-of-flight is inverted

time of flight in scintillators was calculated and how the MUSIC position correction was performed. For more information on particle identification in our experiment we refer to Subsection 3.3.3.

4.3.1 Time of Flight in Scintillators

As was mentioned above, the ideal way of treating the time-of-flight between Sc21 and Sc41 would be to average the time differences from the right to the left sides of the scintillators. Since the resolution of the left-left measurement was poor, we decided to keep only the right-right time difference. Depending on ion trajectories, this can induce systematic shifts in the final quantities. It affects directly the measurements of the velocity and therefore also β (that is the speed of the ions relative to the speed of light v/c), the Lorentz factor $\gamma \equiv 1/\sqrt{1-\beta^2}$, and finally the A/Q ratio (see Section 4.3.5). Nonetheless this approach certainly provided us with the best possible overall measurements.

For the calibration of the T_{flight} , we used several primary beam energies, corresponding to different primary values of β s calculated between Sc21 and Sc41 that we will call β'_{S2-S4} since they are used only for fitting. These β'_{S2-S4} are not the same as β_{S2-S4} , which is the relative velocity of the ions between the S2 and S4 planes, used to calculate the proton number (see Section 4.3.3) and the mass over charge ratio (see Section 4.3.5). Then a linear fitting with parameters C_0 and C_1 was performed with the form:

$$|T_{\text{flight}}| \cdot \beta'_{S2-S4} = C_0 + C_1 \cdot \beta'_{S2-S4}. \quad (4.1)$$

Here both C_0 and C_1 have a special meaning. C_0 is the average flight path divided by the velocity of light. C_1 is an offset value for the time of flight. These parameters are used in order to calculate the value of β_{S2-S4} . This is done through the equation:

$$\beta_{S2-S4} = \frac{C_0}{|T_{\text{flight}}| - C_1} \quad (4.2)$$

4.3.2 MUSIC Position Correction

The unprocessed MUSIC energy loss depends on the particles' velocity. In principle there should also be an effect of two factors on our measurements that have to be cancelled out in order to improve the MUSIC energy loss calculations: the interaction point and the angle of the trajectories.

The position dependence can be derived by illuminating the MUSIC detector and the calibrated position-sensitive detectors with a defocused primary beam. A correction polynomial is made to fit the dependence of the energy loss in the MUSIC with the x position of the interaction point.

For a MUSIC detector in S4, $d_{\text{MW41-MUSIC}}$ is defined as the distance between MW41 and the center of the MUSIC detector. For the MUSIC x position we have (this was done for both MUSIC detectors):

$$x_{\text{MUSIC}} = x_{\text{MW41}} - (x_{\text{angle}} * d_{\text{MW41-MUSIC}}), \quad (4.3)$$

where x_{MW41} is the absolute x position in MW41 and x_{angle} is the x angle in S4. In our case a fourth-order correction polynomial with parameters a_0 , a_1 , a_2 , a_3 , and a_4 was used:

$$x_{\text{correction polynomial}} = a_0 + a_1 \cdot x_{\text{MUSIC}} + a_2 \cdot x_{\text{MUSIC}}^2 + a_3 \cdot x_{\text{MUSIC}}^3 + a_4 \cdot x_{\text{MUSIC}}^4. \quad (4.4)$$

And so we apply the correction in order to cancel out the position dependence and have this new term for the energy loss:

$$\text{MUSIC}_{\text{position corrected energy loss}} = \text{MUSIC}_{\text{energy loss}} \cdot a_0 / x_{\text{correction polynomial}}. \quad (4.5)$$

4.3.3 Proton Number Z

In order to compute the proton number Z , the primary beam Z_{prim} (obtained as the ratio of the measured MUSIC energy loss of the fragment and a primary ion beam having the same velocity as the fragment) and a velocity-dependent correction factor are needed. Using the standard FRS calibration by mapping out the response of the MUSIC chamber to primary beam particles for different energies the calibrated energy loss is written as a second-order polynomial of the β variable (with b_0 , b_1 , and b_2 being adjustable parameters):

$$\text{MUSIC}_{\text{primary energy loss}} = b_0 + b_1 \cdot \beta + b_2 \cdot \beta^2. \quad (4.6)$$

The energy loss in the MUSICs is determined by taking the eighth root of the product of the eight parts of the MUSIC detectors:

$$\text{MUSIC}_{\text{energy loss}} = \sqrt[8]{\prod_{i=1}^8 \text{MUSIC}_{\text{energy loss}_i}}. \quad (4.7)$$

The justification for using such a methodology is that with this way of calculating we increase the coherence of the signals. To illustrate this we show a plot with the energy loss signals coming from the two MUSIC detectors (see Figure 4.2). In both cases a single ΔE signal is plotted in black, while the $\text{MUSIC}_{\text{energy loss}}$ is plotted in blue. We can see that indeed this energy loss signal increases the coherence between the signals. The higher the number of signals the more coherence there will be between them.

The raw Z is obtained with the equation:

$$Z_{\text{raw}} = \sqrt{Z_{\text{prim}}^2 \cdot \text{MUSIC}_{\text{energy loss}} / \text{MUSIC}_{\text{primary energy loss}}}. \quad (4.8)$$

In order to obtain a normalized Z , a linear correction was applied:

$$Z_{\text{norm}} = Z_{\text{raw}} \cdot Z_{\text{slope}} + Z_{\text{offset}}, \quad (4.9)$$

with Z_{slope} , and Z_{offset} being parameters. Our final energy loss is obtained by multiplying the Z calculated in detector MUSIC41 times the Z in MUSIC42 and taking the square root of it:

$$Z = \sqrt{Z_{\text{norm from MUSIC41}} \cdot Z_{\text{norm from MUSIC42}}}. \quad (4.10)$$

4.3.4 Signal in the MUSIC Detectors

Next we show a plot that compares the signals coming from the MUSIC 41 and 42 detectors (Figure 4.3). Even though there are events that could correspond to two different Z values, these are no higher than few tens of counts. We can thus easily make the difference between the different charges due to the good resolution of the MUSIC detectors. To further show this, we also include a plot where we compare the two final Z signals for both detectors. In Figure 4.4 the two signals are plotted together.

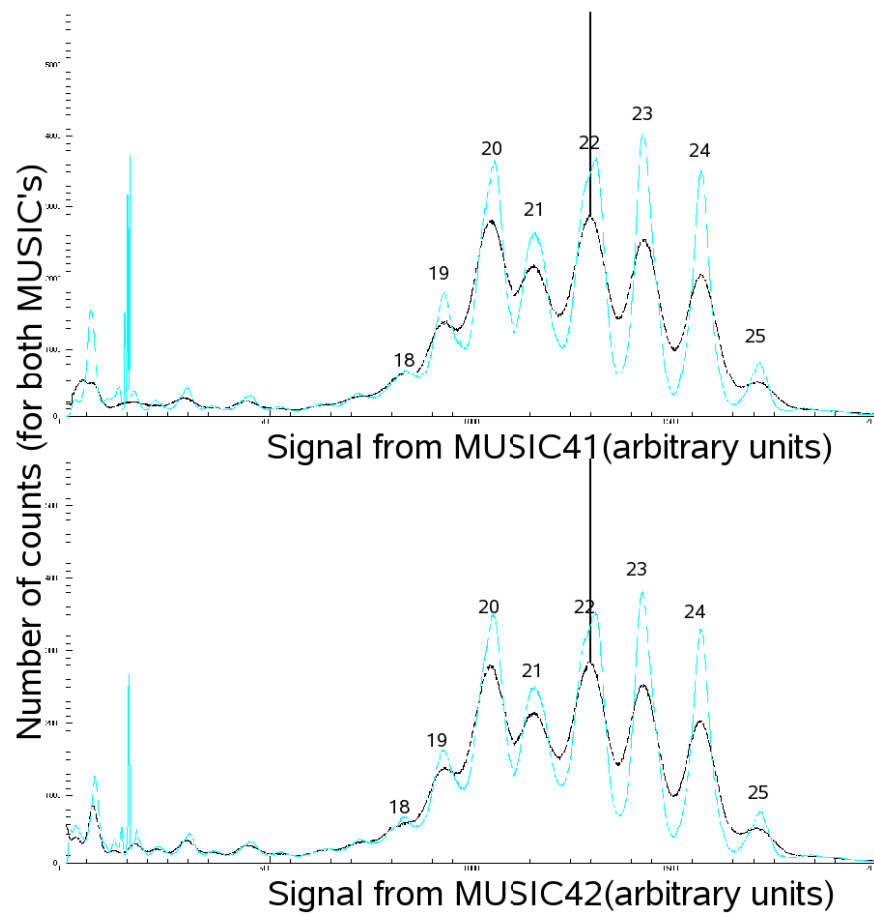


Figure 4.2: Energy loss signals in MUSIC41 and MUSIC42. For both cases the black line is the signal from a randomly selected section of the MUSIC, while the blue line is the $\text{MUSIC}_{\text{energy loss}}$, calculated with Equation 4.7. The unusual spike close to the $Z = 22$ peak seen for both plots is an artifact from the programming. This spike does not appear in the final $\text{MUSIC}_{\text{energy loss}}$ curve

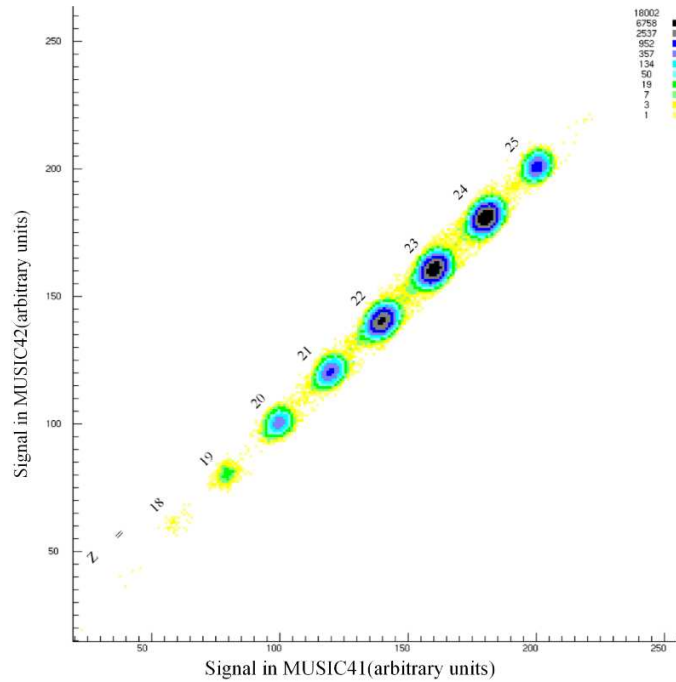


Figure 4.3: A comparison of the two MUSIC signals. It can be seen that the plot is fairly diagonal, and that the different Z 's are recognizable. This is a sign that the charge resolution for our experiment was excellent

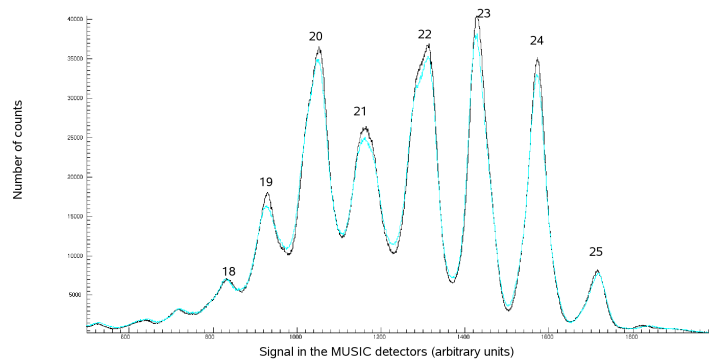


Figure 4.4: Comparison of the two Z signals through the analysis of the MUSIC detectors' signals. MUSIC41 is shown in black, while MUSIC42 is drawn in blue. We can see that the peaks of MUSIC41 are slightly more pronounced than in MUSIC42. This is due to the fact that the signal is damped between the detectors that are between them. The eight Z values of our interest are highlighted again.

4.3.5 Mass-to-charge ratio A/Q

For the calculation of A/Q , several constant properties of the FRS are to be taken into consideration. Amongst them are the effective average dipole radii for the first and second halves of the separator, the magnification, $\text{Mag}_{(S2-S4)}$, and dispersion, $\text{Disp}_{(S2-S4)}$, parameters, which are obtained by beam optics.

In order to calculate the mass-to-charge ratio we also need the time-of-flight and x -positions for each heavy ion at the two focii S2 and S4. The positions in the x axis for the second and fourth sections are called x_2 and x_4 , respectively. These x_2 and x_4 are determined from SC21 and MW tracking, respectively.

Using optics parameters, radii and magnetic-field values, the average magnetic rigidity, B_ρ , values are determined. For S2-S4 we obtain[13]:

$$B_{\rho_{S2-S4}} = B_{S2-S4} \cdot \rho_{S2-S4} \quad (4.11)$$

where B_{S2-S4} is the average of the effective dipole radii of the first and second halves of the separator ($B_{\text{FRS}(3)}$ and $B_{\text{FRS}(4)}$, respectively):

$$B_{S2-S4} = \frac{(B_{\text{FRS}(3)} + B_{\text{FRS}(4)})}{2}, \quad (4.12)$$

and ρ_{S2-S4} is the flying path through the second half of the FRS:

$$\begin{aligned} \rho_{S2-S4} &= \frac{1-\xi \cdot \psi}{2}, \text{ with:} \\ \xi &= \frac{x_4 - x_2 \cdot \text{Mag}_{S2-S4}}{1000 \cdot \text{Disp}_{S2-S4}}, \text{ and} \\ \psi &= \rho_{\text{FRS}(3)} + \rho_{\text{FRS}(4)}. \end{aligned} \quad (4.13)$$

Now, A/Q is finally given by:

$$A/Q = \frac{B_{\rho_{S2-S4}}}{\beta_{S2-S4} \cdot \gamma \cdot u/c}, \quad (4.14)$$

where $\gamma = \sqrt{1/(1 - \beta_{S2-S4}^2)}$, $u=931.49432 \text{ MeV}/c^2$ is the atomic mass unit, and $c=299.792458 \text{ m/s}$ is the speed of light.

As was mentioned in Chapter 3, the x_2 positions for LISE++ are inverted, and thus the term x_2 in Equation 4.13 should have its sign changed for LISE++ computations.

4.4 Comparison of the Ti Positions

LISE++ has been our tool for predicting the outcoming of our experiment. It is interesting for us to compare the location of the elements both in the data analysis and in the LISE++ simulations. For this we choose the Ti ions. In Figures 4.5 to 4.8

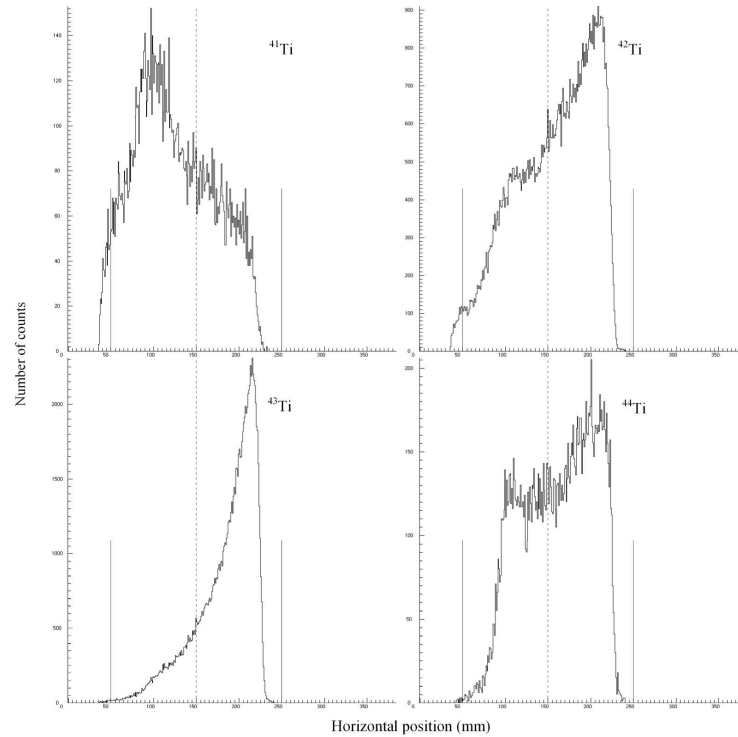


Figure 4.5: Plot of the x_2 position of Ti. The average positions are in Table 4.2. All positions are the channel value of the x axis -150 mm. The dashed lines are positioned in the center. Slits were located in ± 100 mm and represented with continuous vertical lines. Compare these positions to the ones in Figure 4.6.

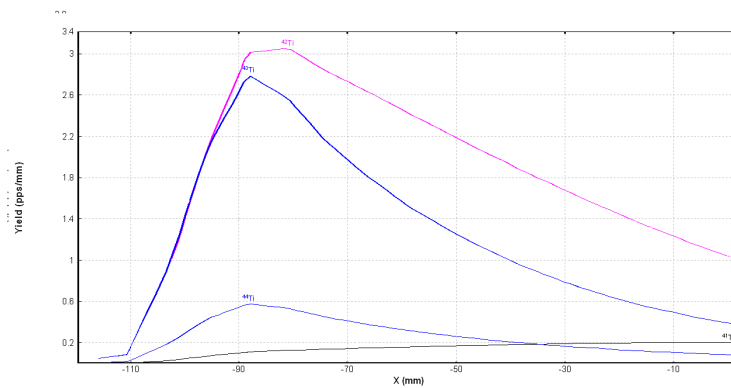


Figure 4.6: Plot of the position of Ti in S2 as predicted by LISE++. The average positions are in Table 4.2.

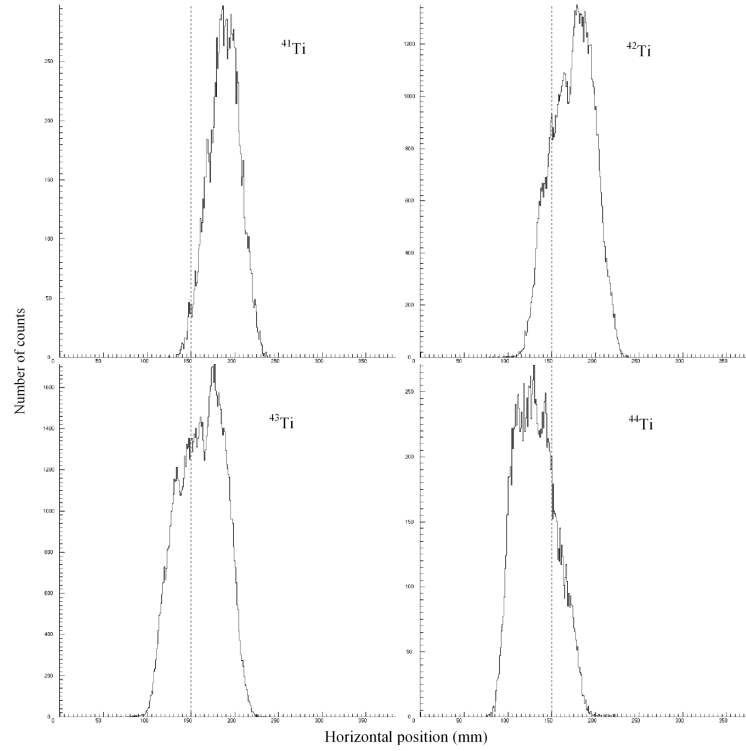


Figure 4.7: Plot of the x_4 position of Ti. The average positions are in Table 4.3. All positions are the value in the x axis -150 mm. The dashed lines are positioned in the center. Compare these positions to the ones in Figure 4.8.

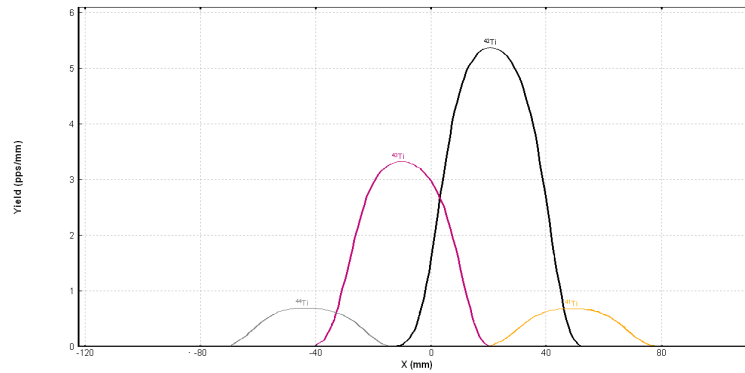


Figure 4.8: Plot of the position of Ti in s4 as predicted by LISE++. The average positions are in Table 4.3.

we show the position of the isotopes both in x_2 and x_4 .

Table 4.2: Comparison of the x_2 centroid positions to the predicted ones by LISE++ and MOCADI. All the positions are written in millimeters relative to the central trajectory. Note that the Data Analysis positions are inverted with respect to Figure 4.5.

Isotope	- Data Analysis	LISE++	MOCADI
^{41}Ti	25.8	1.2	28.4
^{42}Ti	-7.4	-42.6	-44.3
^{43}Ti	-35.4	-57.3	-69.0
^{44}Ti	-11.2	-56.8	(not simulated)

Table 4.3: Comparison of the x_4 centroid positions to the predicted ones by LISE++ and MOCADI. All the positions are written in millimeters relative to the central trajectory.

Isotope	Data Analysis	LISE++	MOCADI
^{41}Ti	37.7	48.8	43.5
^{42}Ti	24.2	21.4	13.2
^{43}Ti	11.5	-9.5	-17.9
^{44}Ti	-17.9	-42.8	(not simulated)

We also have the support of MOCADI simulations [10]. In Tables 4.2 and 4.3 we show the comparison of the positions of the four Ti isotopes in the data analysis, in LISE++, and MOCADI.

As we can see in all these figures, the predicted values of x_2 are clearly not in accordance with the experimental results. This is obvious because neither of the simulations included slits located at S2.

For x_4 positions we can see that indeed there could perfectly be a correlation if one considers that there is a shifting and a shrinking effect in the transformation from the computer simulations to the actual experiment. If we trace such curves we obtain that for LISE++:

$$x_4 \text{ in LISE++} = 1.64 \cdot x_4 \text{ in D.A.} + 18.2 \text{ mm} \quad (4.15)$$

with a coefficient of determination $R^2=0.9674$. While for MOCADI

$$x_4 \text{ in MOCADI} = 2.34 \cdot x_4 \text{ in D.A.} + 44.4 \text{ mm} \quad (4.16)$$

with a coefficient of determination $R^2=0.9994$.

4.5 Development of Track1 and Track2

The data of the experiment was handled in two ways: **Track1** comprises the data with and without the MW signals. **Track2** comprises the full tracking of the ions, i.e., with valid signals from the MW detectors. The reason for considering both is that signals coming out of the MWs were often too small, leading to a lower number of events.

The fact that the signals were unusually diminished in the MW detectors for **Track2** compared to **Track1** could be attributed to the fact that the pressure in the gas chambers was not the proper one for allowing our relatively light ions to induce a signal above the electronics' threshold. Note, however, that in principle the MW signals are necessary for proper A/Q determination (see Section 4.2.5)

Since, as said before, the signal coming out of the MWs was so weak, we preferred to utilize some kind of pseudo tracking without the MWs in order to analyze γ -ray results with better statistics. To obtain the **Track1** matrices a correlation of events between the two trackings was carried out. The main inconvenience of this is that the real trajectory of the individual ions had to be simulated. The events that were detected at S2 and did not leave a sufficiently large amplitude after the MWs were assigned the average x_4 position calculated from the full tracking. In Figure 4.9 we show an example of how the positions looked like in **Track1** and **Track2**

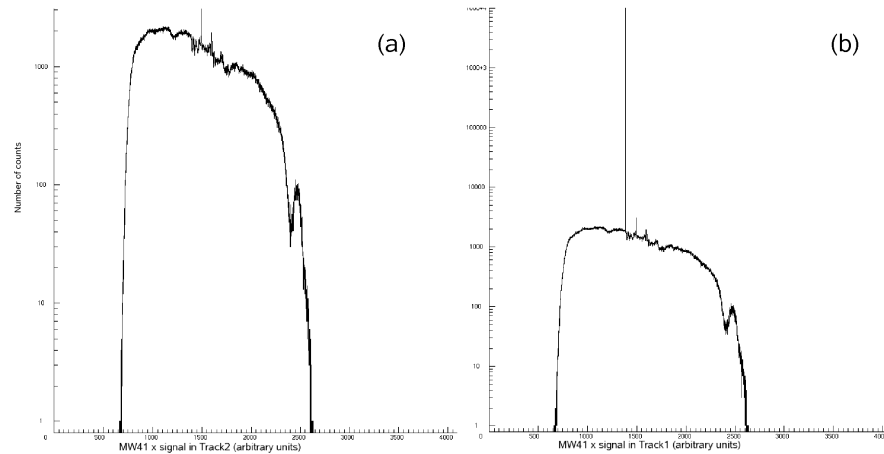


Figure 4.9: The signal from MW's 41 in **Track2** on the left, and **Track1** on the right side. Note how in **Track1** the average position is added a very big amount of events that are not present in **Track2** (it is several orders of magnitude higher than any of the channels in the full tracking). A logarithmic scale is used in both cases.

Let us first show an example of how much the difference in number of events was between the two data samples. We show the plots of Z vs A/Q for the two tracks in Figure 4.10. The overall difference in statistics is around 4.6.

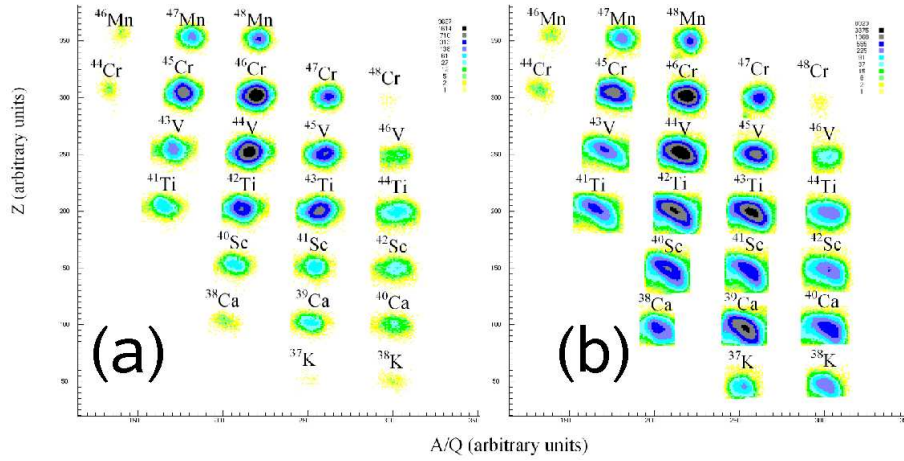


Figure 4.10: This plot shows position in Z vs A/Q contained in the two tracks. (a) shows the data from **Track2** and has 1,170,000 events. (b) contains the data from **Track1** and has a total summation of 5,380,000. The overall relation between both statistics is about 4.60.

For this experiment, 24 nuclei are to be studied. Table 4.3 shows the number of ions for the two types of data handling. We want to see if the proportion between the statistics depends directly on the charge of the nucleus:

We can see in Figure 4.10 and Table 4.5, that the first evident behaviour is that the higher the Z number, the lower the ratio (as predicted by the Blethe-Bloch formula). But we can also appreciate that for the elements with the lowest Z (elements with the highest ratio), that ranged from K to Ti the ratio is not the same for isotopes with the same charge. The first thing one could argue for, is that the events in **Track2** are so sparse that they cannot be considered statistically. The other important justification for such a behaviour is that mass does play a certain role, especially for the nuclei with the lowest charge. We can see in all of these that for a constant Z , the higher the mass of the isotope the smaller the ratio. Ions with the same charge but with different masses will have different kinetic energies. If they are all given the same velocity, it is reasonable to think that heavier ions will have higher kinetic energies and therefore will be harder to intersect in the MW's, causing a higher ratio.

For the isotopes from V to Mn the ratio is practically uniform for every charge. In these cases the ion mass does not seem to exercise much influence in the difference in statistics.

Table 4.4: Comparison in the number of statistics between **Track1** and **Track2** for each studied isotope

Nucleus	Counts in Track1	Counts in Track2	Ratio
³⁷ K	25,700	46	≈ 559
³⁸ K	64,600	350	≈ 185
³⁸ Ca	118,000	873	≈ 135
³⁹ Ca	586,000	8,990	≈ 65.2
⁴⁰ Ca	189,000	4,440	≈ 42.6
⁴⁰ Sc	251,000	10,600	≈ 23.7
⁴¹ Sc	190,000	11,200	≈ 17.0
⁴² Sc	95,800	8,320	≈ 11.5
⁴¹ Ti	121,000	13,000	≈ 9.31
⁴² Ti	593,000	81,500	≈ 7.28
⁴³ Ti	612,000	112,000	≈ 5.46
⁴⁴ Ti	76,600	15,900	≈ 4.82
⁴³ V	88,400	23,600	≈ 3.75
⁴⁴ V	941,000	289,000	≈ 3.26
⁴⁵ V	217,000	73,000	≈ 2.97
⁴⁶ V	11,700	3740	≈ 3.13
⁴⁴ Cr	1,360	584	≈ 2.33
⁴⁵ Cr	287,000	116,000	≈ 2.47
⁴⁶ Cr	750,000	322,000	≈ 2.33
⁴⁷ Cr	79,700	34,400	≈ 2.32
⁴⁸ Cr	210	57	≈ 3.69
⁴⁶ Mn	802	372	≈ 2.16
⁴⁷ Mn	34,000	16,500	≈ 2.06
⁴⁸ Mn	49,700	23,800	≈ 2.09

Chapter 5

Isomer Study

The present chapter explains how the isomer study was performed by investigating the energy vs time matrix for each isotope. The first section intends to probe the common characteristics of all the E_γ vs t matrices, using isotopes that do not have any isomeric states. Sections 5.2, 5.3, and 5.4 discuss the identification of isomeric transitions in ^{43}Ti , ^{38}K , and ^{45}Cr , respectively. The fourth section describes the half life calculation for a given isomeric state.

5.1 Isotope-Gated γ Analysis

After the isotope identification was done, it is possible to “gate” on the different isotopes in order to obtain an energy vs time matrix for each ion. Further information on the isotope identification can be found in Chapter 4. To gate means that we only select the events that match certain criteria. In Figure 4.10(b), we can consider all the γ -ray decays that correspond to a specific “blob”, and study it separately from the others. This is thus called an isotope-based gating.

Before studying the isomers, an abundant isotope with no known or expected isomers, for instance, ^{44}V is examined. Matrices of such isotopes can facilitate identification of non-isomeric transitions from, for example, background radiation in the experimental area or specific to the experimental technique. When comparing to spectra from nuclei with isomeric transitions it will be easier to identify the peaks from the decay of the isomeric states.

An energy-time matrix is used to observe isomeric states of the implanted isotopes. After the time of implantation of the fragments in the stopper and its corresponding “flash” due to the ionization and emission of bremsstrahlung have occurred, other peaks with a long enough lifetime as to outlast this glint can be visually differentiated in the spectrum.

In order to analyze the isomeric states three different time ranges were used: The long range, also called **1L**, consisting of a resolution of 200 ns per channel; the medium range, **aM**, with a resolution of 25 ns per channel; and the short range, **aS**,

10 ns per channel. Throughout this work we will show only the results from the long (1L) and the medium (aM) ranges. The short range was not used in the present work.

In Figures 5.1 and 5.2 the ^{44}V -gated E_γ - t plots for long and medium time-ranges, respectively, are displayed. In both cases the vertical high intensity band corresponds to the time of implantation and its remnants. We can appreciate horizontal lines, that could be either due to natural background radiation or to γ rays from natural reactions that occur between neutrons produced in nuclear reactions and the germanium present in the detectors, $^{\text{nat}}\text{Ge}(n,n'\gamma)$. According to literature, [14], the most important transitions for this kind of reaction will have energies of 596 keV and 692 keV for ^{74}Ge and ^{72}Ge , respectively. The other abundant isotope of Ge, ^{73}Ge , has a peak with an energy of 894 keV, but it is not clearly seen for any of the two ranges after the implantation “shine”. All horizontal lines except for the ones from natural background origin have decreasing intensity, as will the isomer-originated lines.

Additional gating can be performed in a γ -ray spectrumsubtractm, i.e., number of counts as a function of E_γ in order to cut out the time of implantation and look at the energy of isomeric transitions more easily. In Figure 5.3 the projection of the times shown in 5.1 and 5.2 are traced in a number of counts vs E_γ graphic. The identified background energies were 511 keV, which corresponds to the annihilation of positronium (e^+e^-); 609 and 1765, ^{214}Bi ; 911 keV, ^{228}Ac ; 1461 keV, ^{40}K ; and 2615 keV, ^{208}Tl . The last five background energies correspond to elements that are present in the walls or in other parts of the components in the detection devices. It is worth mentioning that many of these are rather hard to perceive visually, since their intensity is so small, therefore a time projection like the one in Figure 5.3 helps us to visualize them better.

A projection of times that does not include the “prompt flash” –and sometimes short-lived isomers– can be executed for the same isotope in order to obtain a cleaner spectrum that contains as many γ 's from isomeric decays as possible. A gating of an isotope with no seen transitions from isomeric states can be carried out between the same initial and final times in order to normalize and then subtract it from the original one in order to cancel out the background. For more information on this background and other isotopes normalized subtraction see Sections 5.2, 5.3, and 5.4.

5.2 ^{43}Ti analysis

One of the isotopes that was expected to have isomeric transitions was ^{43}Ti . Considering the lifetimes of the isomers in ^{43}Ti , the isomeric transitions were studied both for the long and for the medium ranges. In Figure 5.4 we show the relevant part of the level scheme of ^{43}Ti [14].

5.2.1 Long Time Range Analysis

In the case of ^{43}Ti , the isomeric transition of interest for the long range is the 313 keV line. To isolate this “line” a time gate for which the other isomeric transitions' intensities are insignificant was executed. This was possible since the lifetimes for the

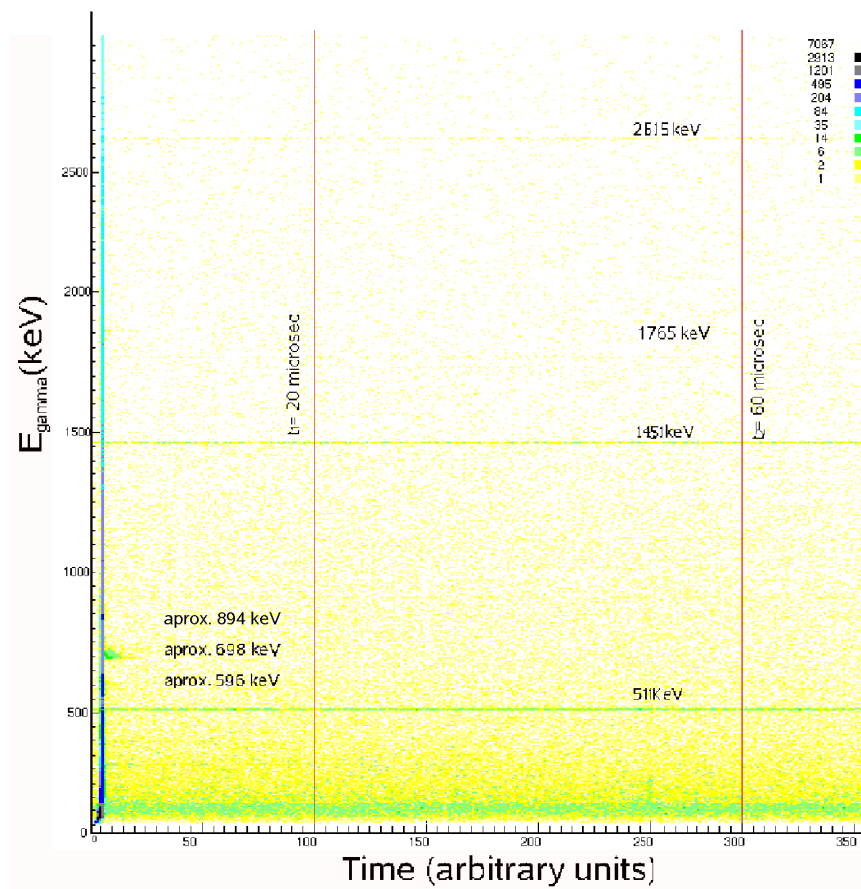


Figure 5.1: The energy vs time matrix for ^{44}V for the long range (a resolution of 200 ns per channel). Background and $^{\text{nat}}\text{Ge}(n,n'\gamma)$ (around 596, 698, and 894 keV) energies are identified. An example of a gate is traced in red between times $t_1 = 20\mu\text{s}$ and $t_2 = 60\mu\text{s}$. In this gate interval it was intended that the $^{\text{nat}}\text{Ge}(n,n'\gamma)$ reactions were cut out.

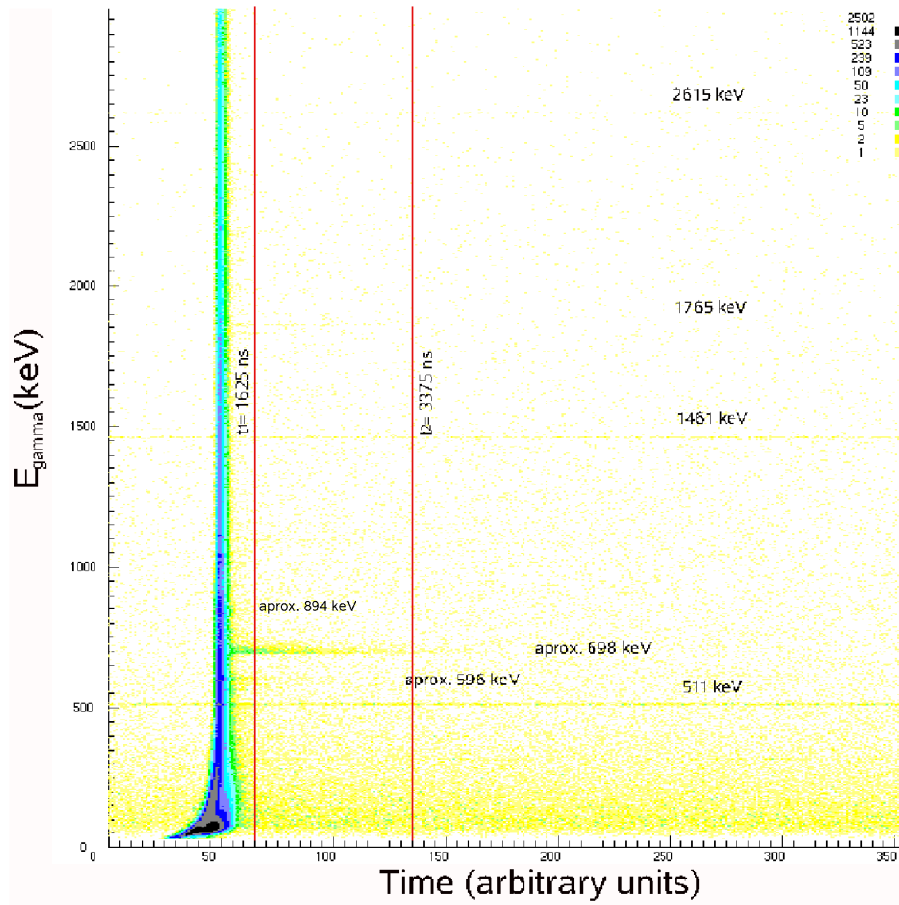


Figure 5.2: The energy vs time matrix for ^{44}V for the medium range (a resolution of 25 ns per channel). Background and lines from $^{\text{nat}}\text{Ge}(n,n'\gamma)$ reactions (around 596, 698, and 894 keV) energies are identified. Note that background lines are visible before the time of implantation. An example of a gate is traced in red between times $t_1 = 1625 \text{ ns}$ and $t_2 = 3375 \text{ ns}$. In this interval the $^{\text{nat}}\text{Ge}(n,n'\gamma)$ reactions are included.

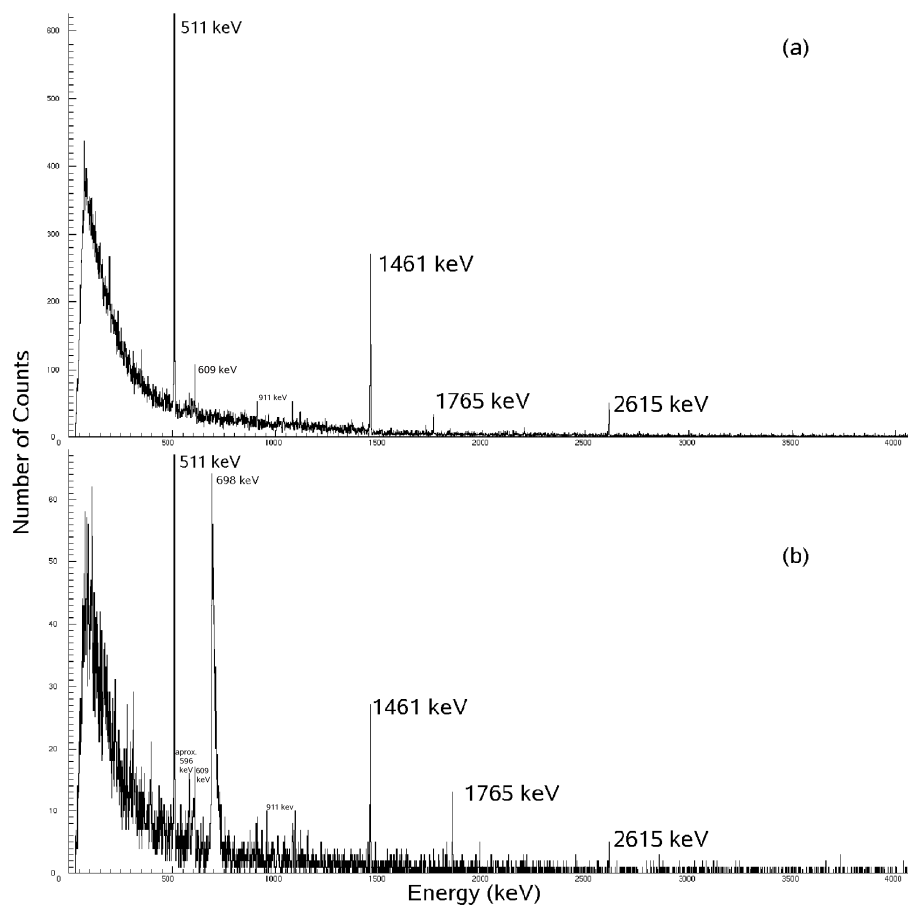


Figure 5.3: Spectrum for ^{44}V . In (a) and (b) we see the spectrum between the marked intervals for the long and the medium range, respectively. Note how in (a) (time interval from $t_1 = 20\mu\text{s}$ to $t_2 = 60\mu\text{s}$) the lines due to $^{\text{nat}}\text{Ge}(n,n'\gamma)$ reactions have practically no counts, while in (b) (from $t_1 = 1625\text{ ns}$ to $t_2 = 3375\text{ ns}$) the 596 keV reaction has a considerable intensity with respect to the background energies for, as can be seen in Figure 5.2, the gate includes counts from these reactions inside the detectors. The origin of all the identified background lines is explained in the text.

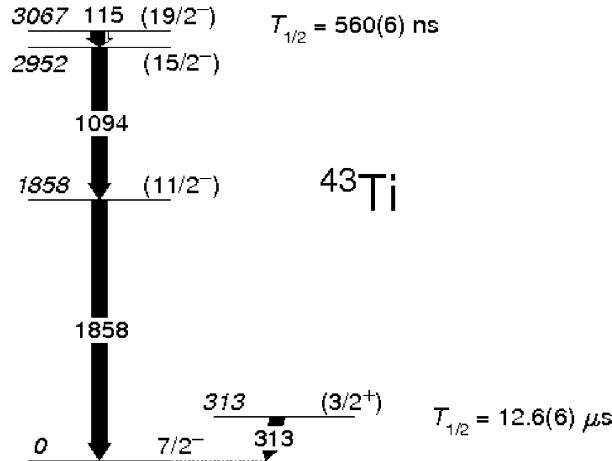


Figure 5.4: Relevant part of the level scheme for ^{43}Ti [14]. Only the expected transitions, with the half-lives taken from the literature, are shown.

Ge reaction and other isomeric transitions were smaller.

In Figure 5.5 the long range E_γ - t plot with the gating interval between $t_1 = 6\mu\text{s}$ and $t_2 = 66\mu\text{s}$ after the prompt flash limits is drawn. Note that with this gating on time we can cut out the prompt flash, the Ge transition lines (no further than $2.60\mu\text{s}$), and the other visible isomeric transitions (that had basically disappeared after $6.0\mu\text{s}$). This is seen in Figure 5.6(a), where the only seen peaks correspond to background lines and the 313 keV isomeric transition.

With the gating described above, we can obtain a raw spectrum that still contains the lines due to the natural background. Our purpose now is to refine this spectrum so we can find the best, clean spectrum for our isomeric transition. In order to do this, the first possible method is to do a gating for the same amount of time in the ^{43}Ti E vs t matrix in a subsequent time from 66 to $126\mu\text{s}$ when the 313 keV line has basically disappeared. Then we do a subtraction of this raw time from the background, and we are left with the much cleaner spectrum in Figure 5.6(b).

Another option available is to take two (or more) prolific nuclei that do not present any isomers. In our case ^{42}Ti and ^{44}V were chosen, since they are rather abundant in the experiment. After gating on the two in the same time interval, and adding their spectra to obtain a new spectrum, we sum the intensity of this obtained spectrum in the 511 keV peak. We make the same integration for the ^{43}Ti spectrum. We obtain the ratio of the new spectrum 511 keV peak intensity, as compared to the ^{43}Ti , and we divide the new spectrum by this ratio. With such a procedure we normalize the ^{43}Ti and the $^{42}\text{Ti} + ^{44}\text{V}$ spectra to background radiation, and then we subtract them so the resulting spectrum will have all the background lines canceled out. The results of this procedure can be seen in Figure 5.6(c). By looking at the plots one can see that both the background subtraction and the comparison to isotopes with no isomers

help us obtaining sufficiently clean spectra.

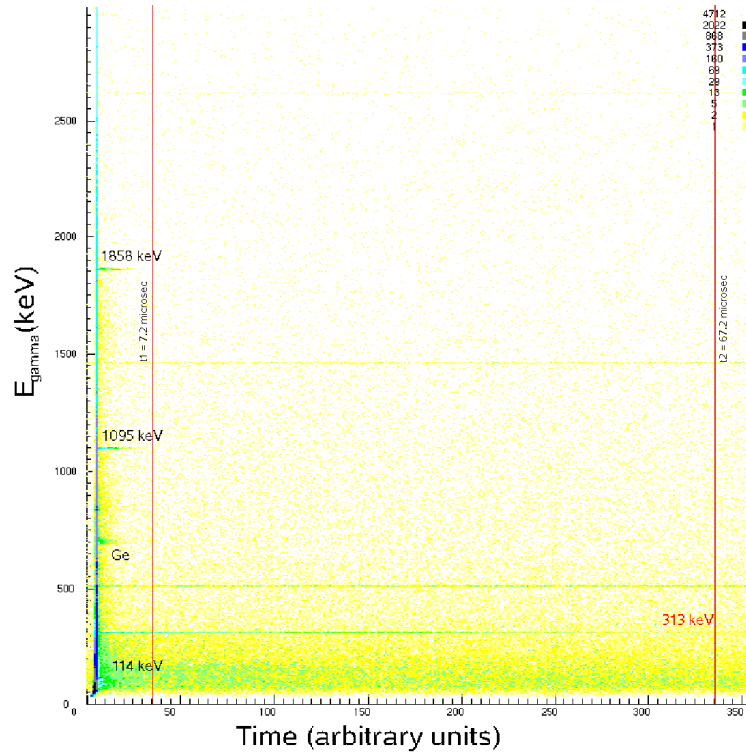


Figure 5.5: The long range E_γ vs time plot for ^{43}Ti . The limits for the gating between $t_1 = 7.2\mu\text{s}$ and $t_2 = 67.2\mu\text{s}$ are painted in red (6 and 66 $7.2\mu\text{s}$ with respect to the prompt flash). Note how the 313 keV peak outlives the other isomeric lines and the $^{\text{nat}}\text{Ge}(n,n'\gamma)$ energies.

5.2.2 Medium Time Range Analysis

A similar procedure was done for the medium range. In Figure 5.5 we show the E_γ vs time matrix with the time gating between 0.4 and 2.15 μs highlighted. The main difference between the 1L and the aM analysis for ^{43}Ti is that in the long range analysis it was possible to isolate the 313 keV isomeric line from the other decreasing lines and still collect enough statistics. In the medium range it was impossible to take away the 313 keV isomeric since, as can be seen in Figure 5.7, it was so much longer than the rest. The Ge reactions in the detectors were not taken out either because even though the isomeric lines outlived these Ge energies, it was by a very little margin; therefore including exclusively times after the vanishing of the $^{\text{nat}}\text{Ge}(n,n'\gamma)$ would have led to a very poor collection of statistics.

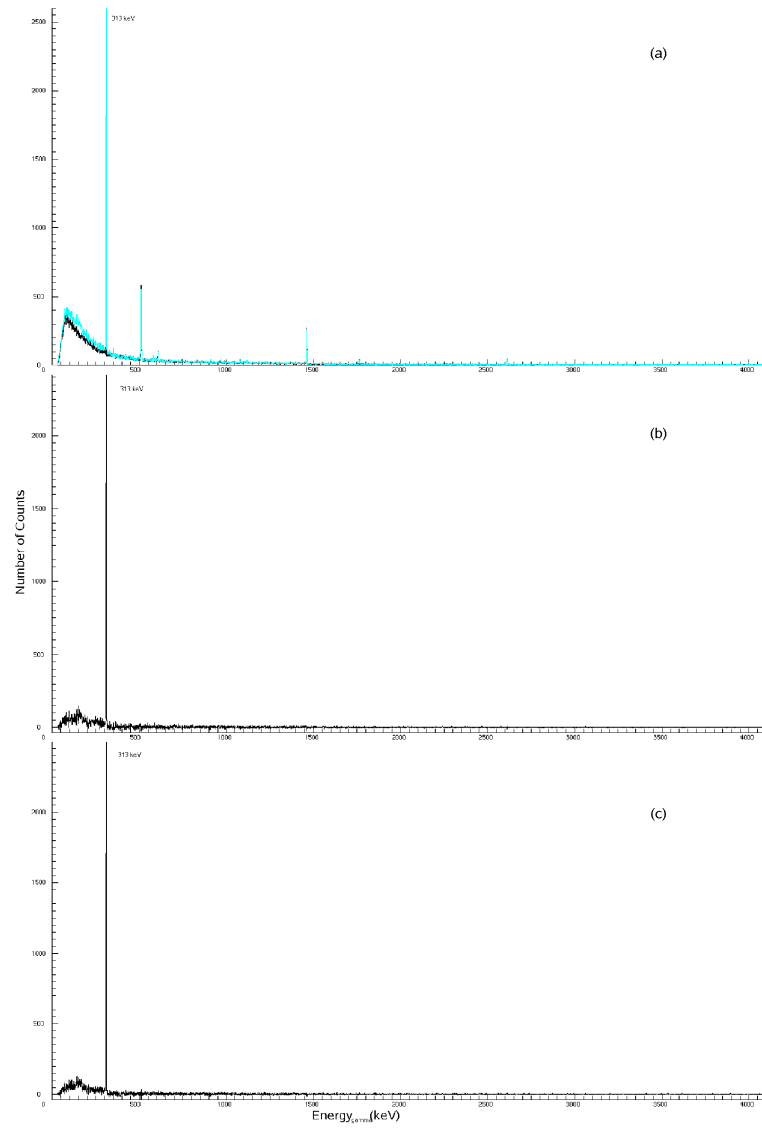


Figure 5.6: A comparison of the two possible methods for obtaining a clean spectrum in the case of ^{43}Ti for the long range. In (a) the raw spectrum (in blue) is plotted together with a background spectrum (in black). The two methods, in (b) and (c), are discussed in detail in the text. Note the 313 keV peak in all three spectra.

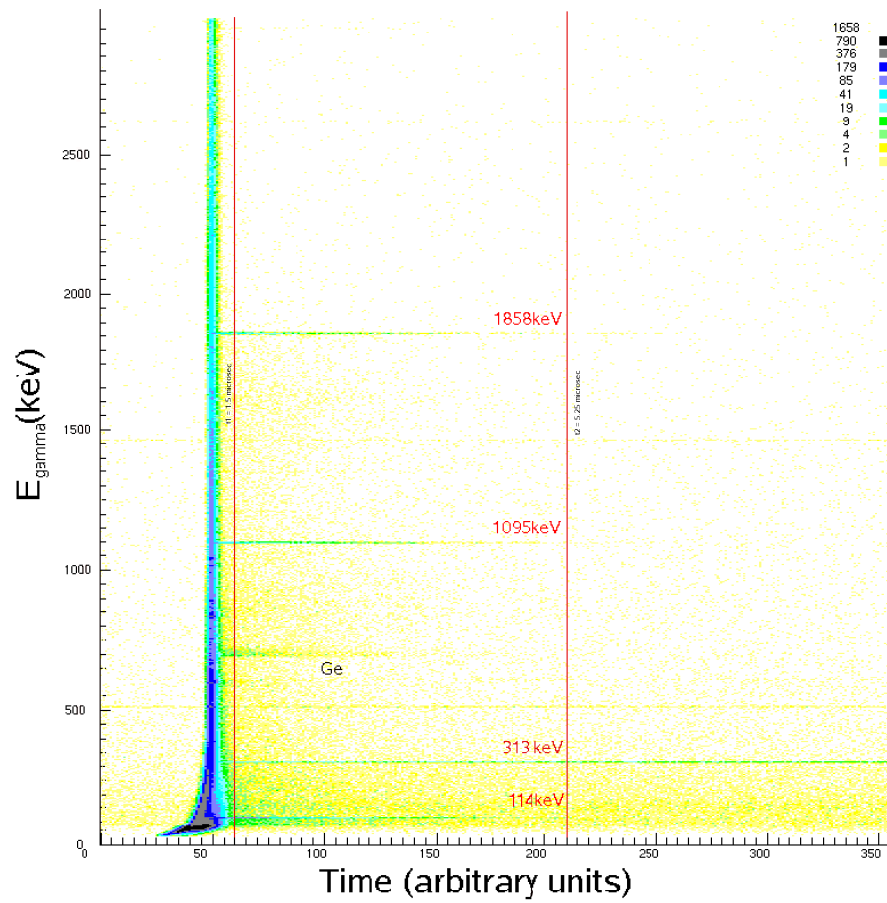


Figure 5.7: The medium range E_γ vs time plot for ^{43}Ti . The limits for the gating in $t_1 = 1.5\mu\text{s}$ and $t_2 = 5.25\mu\text{s}$ (0.275 and $4.125\mu\text{s}$ with respect to the prompt flash) are painted in red. Note that even though the three desired peaks are included in this gating, so are the 313 keV transition (see Section 5.2.1) and the Ge reaction lines (see Section 5.1).

To obtain a cleaner spectrum the method of comparing the desired spectrum with those of isotopes with no seen isomers was chosen. The reason for this selection is that since the Ge decays could not be taken away, by comparing the other elements we can subtract not only the background lines, but also the undesired decreasing lines due to Ge reactions. In Figure 5.8 we can see the spectrum between the chosen time interval that all the peaks, including the 313 keV, are present.

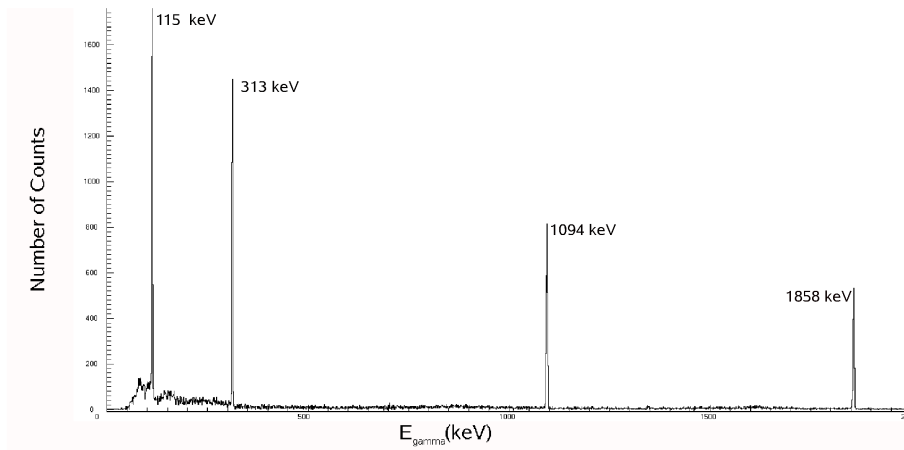


Figure 5.8: The energy spectrum for ^{43}Ti in the medium range for the time gate from $t_1 = 0.275\mu\text{s}$ to $t_2 = 4.125\mu\text{s}$. The seen peaks are, in increasing order, 115 keV, 313 keV, 1094 keV, and 1858 keV.

5.3 ^{38}K

Knowing the half life of our expected isomer, 7^+ , which is illustrated in Figure 5.9, we will only consider the long range resolution. In Figure 5.10 we show both the gating interval and the obtained spectrum after doing a normalized subtraction (cf. Sections 5.1 and 5.2).

5.4 ^{45}Cr

In the case of ^{45}Cr the isomeric states were unknown. Nevertheless an isomeric transition line was expected due to the analogy to its mirror isotope, ^{45}Sc , which decay scheme is depicted in Figure 5.11. In Figure 5.12 the energy vs time matrix is shown for the long range with the corresponding time limits for the gate along with the clean spectrum obtained by using the normalized subtraction method. The spectrum comprises a γ -line from an isomeric decay in ^{45}Cr at 107 keV. For analogy we could believe that this transition is the same transition from $3/2^+$ to the ground state, $7/2^-$.

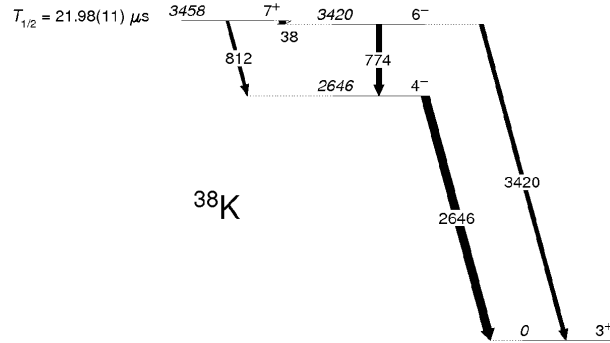


Figure 5.9: Level scheme for ^{38}K . The only expected band, with the half-life taken from the literature, is shown.

5.5 Half Life Calculation

With the aid of the available software we can do an energy gating. With it we can see the evolution in time of the counts for a certain isomeric γ -ray line in a one-dimensional plot. In Figure 5.13 we show a zoomed version of Figure 5.6(c) on the 313 keV line. Areas surrounding the peak are considered in order to have a background spectrum. In Figure 5.14 we show the evolution of an isomeric line in time for the 313 keV line in ^{43}Ti .

In order to calculate the half life, $T_{1/2}$, the prompt flash shall not be considered. The fitting is a least-squares adjustment of the function:

$$N(t) = a_0 \cdot e^{-a_1 \cdot t} + a_2 \quad (5.1)$$

with $N(t)$ being the number of counts, and a_0 , a_1 , and a_2 being parameters. This fitting is performed by using iterations. The process consists of defining a minimum, a maximum value, and a number of iterations for each variable. A Pearson's chi-square test (χ^2) was done for each set of a_0 , a_1 , and a_2 values:

$$\chi^2 = \sum_{i=1}^n \frac{(O_i - E_i)^2}{E_i}, \quad (5.2)$$

where O_i are the observed values for the number of counts and E_i are the estimated ones given by the three a_i . The set of a_0 , a_1 , and a_2 with the lowest χ^2 was taken as the estimated values for these three parameters. The range of each parameter, i.e., the interval between the minimum and the maximum values, was the section around the average where the value of χ^2 was between χ_{\min}^2 and $\chi_{\min}^2 + 1$, having the other two parameters fixed to their estimated values. The half lifetime is computed through the equation:

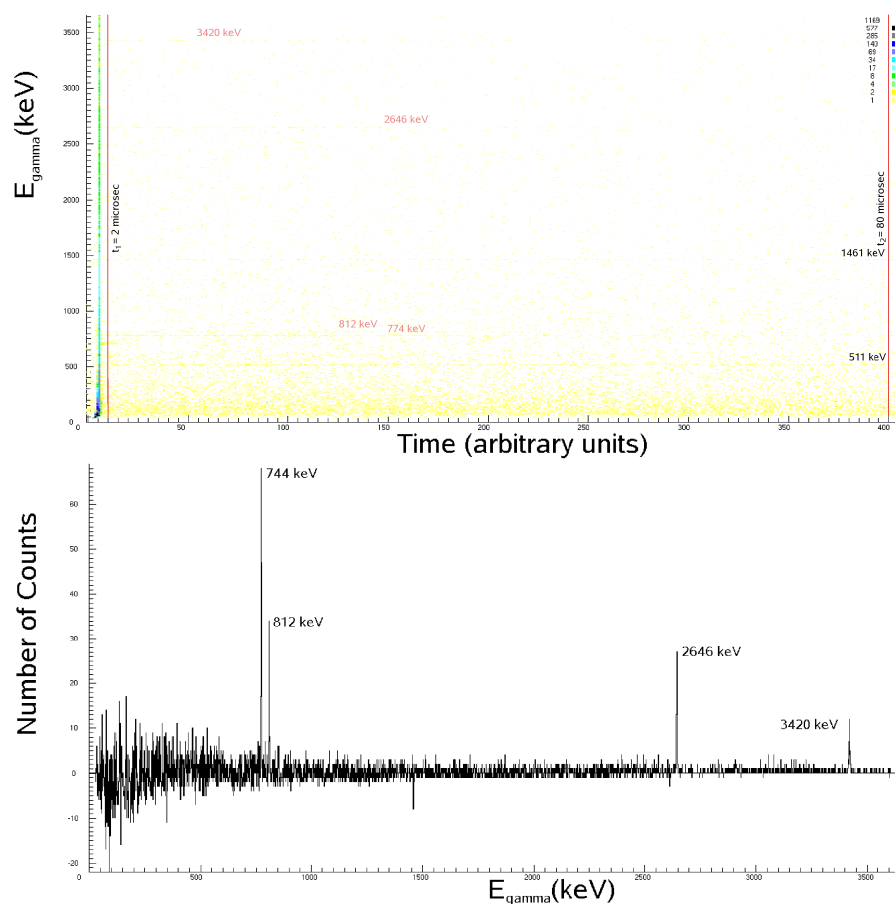


Figure 5.10: Time gate and spectrum for ^{38}K . On top we show the E_γ vs time matrix for the long range with the gate interval from $t_1 = 0.775\mu\text{s}$ to $t_2 = 78.775\mu\text{s}$ (note that they differ from that in the drawing for they were traced with respect to the prompt flash). All visually differentiable energies in this matrix are highlighted in red for the isomeric lines, and in black for the background lines. On the bottom we show the result of this gate and the subsequent normalized subtraction by comparing to ^{44}V and ^{42}Ti . The seen isomeric transitions are, in increasing order, 774 keV, 812 keV, 2646 keV, and 3420 keV.

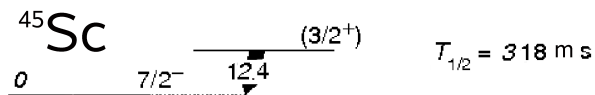


Figure 5.11: Relevant part of the level scheme for ^{45}Sc [14]. Only the transitions of our concern are shown. This is a good indicative for the isomer analysis of its mirror nucleus, ^{45}Cr .

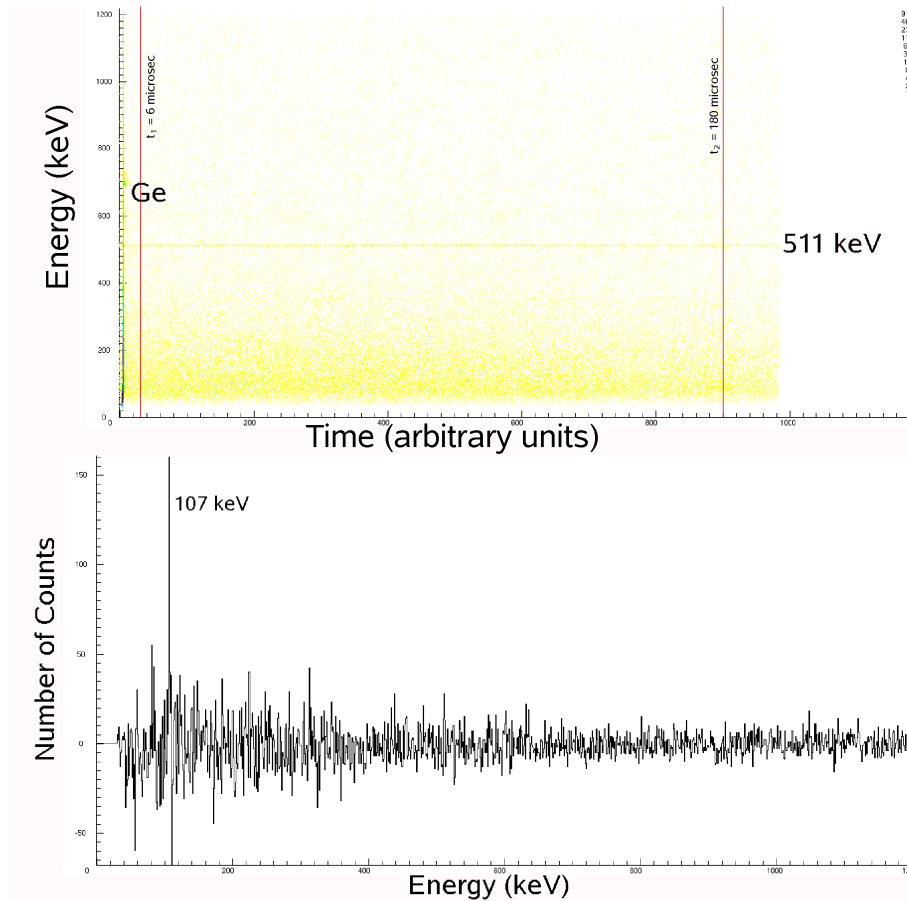


Figure 5.12: Time gate and spectrum for ^{45}Cr . On top we show the E_γ vs time matrix for the long range with the gate interval from $t_1 = 0.775\mu\text{s}$ to $t_2 = 78.775\mu\text{s}$ (note that they differ from that in the drawing for they were traced with respect to the prompt flash). $^{\text{nat}}\text{Ge}(n,n'\gamma)$ and background lines are highlighted on the upper picture. On the bottom we show the result of this gate and the subsequent normalized subtraction by comparing to ^{44}V and ^{42}Ti . The seen isomeric transition is 107 keV. To enhance the appreciation of this picture only the interval from 0 to 1200 keV is shown for it is the only relevant range of energies.

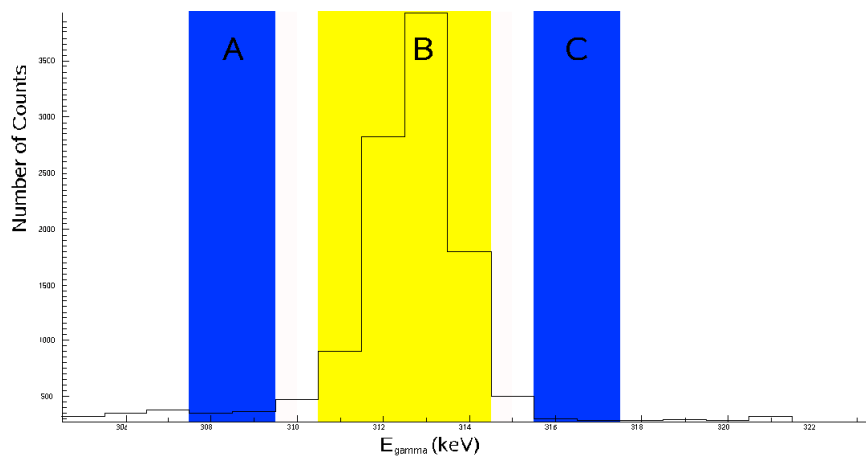


Figure 5.13: Time gating of the ^{43}Ti long range matrix (zoomed near the 313 keV peak). Intervals A and C are taken for being an estimation of the background, while region B is the raw peak. Note that the number of channels of B (four) is equal to the summation of A and C (two each)

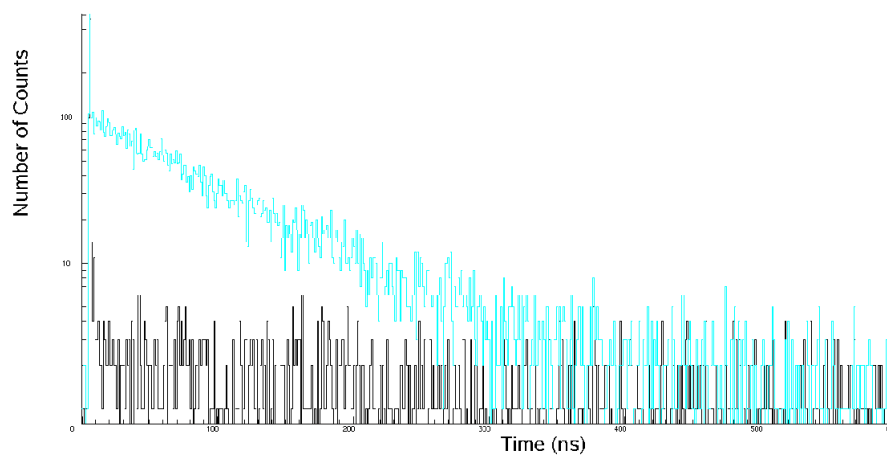


Figure 5.14: Energy gating of the 313 keV peak for ^{43}Ti . Here the area under the peak (area B in Figure 5.5) is drawn in blue and the background (regions A and C) is pictured in black. The process of fitting is explained in the text. The y axis (number of counts) was drawn with a logarithmic scale. Note the prompt flash in the very beginning for both curves.

$$T_{1/2} = \frac{\ln 2}{a_1}. \quad (5.3)$$

5.5.1 ^{43}Ti Isomeric Analysis

In Figure 5.15 we show the evolution in time of the 313 keV peak (the spectrum minus the background) along with an example fit for the long range. Even though one is supposed to include the complete range of events in the fit, it is also true that the selection of the range of the fit plays a role in the final result of the $T_{1/2}$. Therefore, it was decided to probe, in particular to obtain a realistic estimate of the uncertainty, several intervals of channels. In tables 5.1 and 5.2 we show the calculated $T_{1/2}$ with its corresponding individual error for the long and the medium time range, respectively. To obtain an better estimate the minimum and the maximum values are considered to be the interval and the midpoint between them is considered the estimated value. As can be seen in the pictures, the obtained $T_{1/2}$'s are $11.25(13)\mu\text{s}$ and $11.10(26)\mu\text{s}$ for the long and the medium range, respectively.

With the result from the medium and the long range we use the weighted average of them with the equations:

$$\langle A \rangle = \frac{\sum A_i / \Delta A_i^2}{\sum 1 / \Delta A_i^2}, \text{ and} \quad (5.4)$$

$$\Delta \langle A \rangle = \frac{1}{\sqrt{\sum 1 / \Delta A_i^2}}, \quad (5.5)$$

This gives $T_{1/2}$ is $11.20(12)\mu\text{s}$ as a result. Note that it is different from the literature value, $12.6(6)\mu\text{s}$ [14].

For the other peaks, which are best analyzed in the medium range, the lifetime of all of them can help us to find the $T_{1/2}$. We can affirm this because all the states with energies between $19/2^-$ and $7/2^-$ in the same band have short lifetimes. These intermediate states' lifetimes are not known in ^{43}Ti , but we know that $T_{1/2}(11/2^-) = 0.20(3)\text{ps}$ and $T_{1/2}(15/2^-) = 5.6(7)\text{ps}$ for its mirror nucleus, ^{43}Sc [14]. It is logical to think that these states would not make a change relevant to the precision of this experiment. First we show the individual results of the fitting of the 115 keV line in Figure 5.16 and Table 5.3, then the 1094 keV line in Table 5.4, and finally the 1858 keV line in Table 5.5.

To have better statistics we added all the spectra coming from the 115, 1094, and 1858 keV peaks, since, as said before, the lifetimes of the states in between are several orders of magnitude smaller. In Figure 5.17 the spectrum of the addition of all these peaks is shown with an example fit. In Table 5.6 the result of the different adjustments is displayed. We can affirm that such an addition was correct since $T_{1/2}$ was close enough for the three peaks.

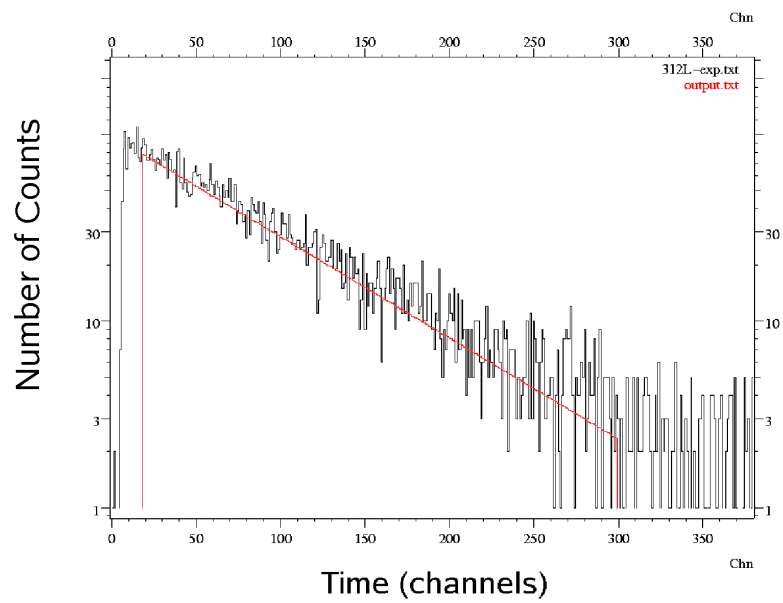


Figure 5.15: The time spectrum for 313 keV (black) and an example of a fit (in red) for a 200ns per channel resolution. The number of counts are drawn in logarithmic scale.

Table 5.1: Result of the fit for different time ranges in the 200 ns resolution for the 313 keV peak in ^{43}Ti . The three bottom ones are not considered since they include not long enough ranges. The 50-700 range, as can be seen in Figure 5.15 does not have a proper section of the beginning of the function while the 20-300 range does not include an important portion of the end of it. This leads to the provisional result of $T_{1/2} = 11.25(13) \mu\text{s}$.

$T_{1/2}(\text{ns})$	ch-low	ch-high
11257(2)	10	800
11200(2)	15	800
11280(2)	20	400
11363(2)	10	400
11200(2)	15	700
11164(2)	20	700
11142(2)	10	900
11090(2)	50	700
11137(2)	20	300

Table 5.2: Result of the fit for different intervals in the medium resolution range for the 313 keV peak. The two bottom ones were not considered. It helps us conclude that $T_{1/2} = 11.10(26) \mu\text{s}$.

$T_{1/2}(\text{ns})$	ch-low	ch-high
11096(3)	70	700
11114(3)	60	780
11360(3)	60	600
11165(3)	50	800
11149(3)	50	780
10833(3)	80	800
11103(3)	70	780
11027(3)	100	780
11296(3)	80	500

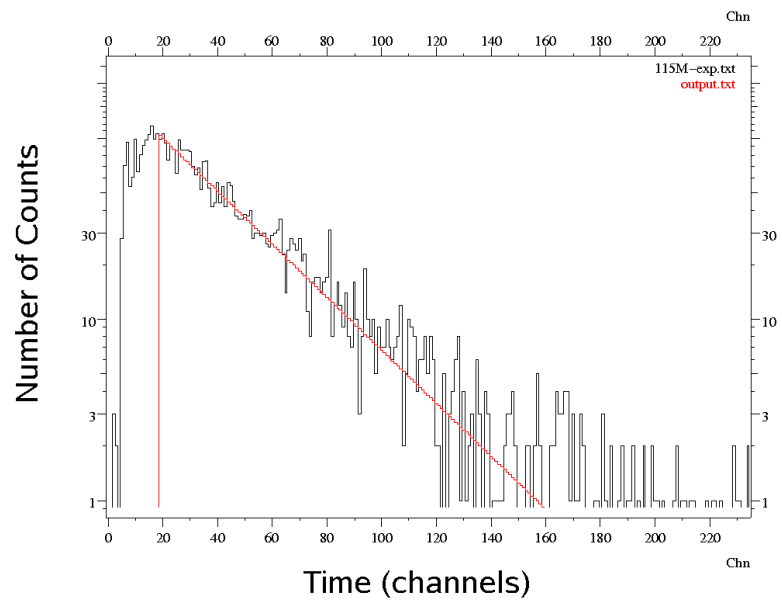


Figure 5.16: Time evolution of the 115 keV peak in the medium range (resolution of 25ns per channel) for ^{43}Ti , along with an example adjustment. The vertical axis uses a logarithmic scale.

Table 5.3: Result of the fit of the 115 keV peak in the medium resolution range for ^{43}Ti . The bottom one was not considered. The result of this adjustment is of 512(5) ns.

$T_{1/2}(\text{ns})$	ch-low	ch-high
505.9(5)	16	120
517.7(5)	16	200
516.8(5)	16	70
521.5(5)	20	160
518.2(5)	20	200
512.2(5)	30	160
511.3(5)	20	120
509.1(5)	30	200
526.7(5)	16	400
506.8(5)	30	70

Table 5.4: Result of the fit on the 1094 keV peak in the medium resolution range for ^{43}Ti . It makes us conclude that the half life time for the $19/2^-$ band is of 545(21) ns, comparable to the 560(6) ns from the literature [14]. The actual plot is not in the text.

$T_{1/2}(\text{ns})$	ch-low	ch-high
524.5(6)	20	140
523.8(6)	10	140
524.5(6)	30	140
549.1(6)	20	100
566.3(6)	10	100
535.5(7)	30	100
526.4(6)	20	160
525.8(6)	10	160
527.0(6)	30	160
526.4(6)	9	180

Table 5.5: Result of the fit on the 1858 keV peak in the medium resolution range for ^{43}Ti . It makes us conclude that the half life time for the $19/2^-$ band is of 480(40) ns, that is not very close to the 560(6) ns from the literature. The actual plot is not in the text.

$T_{1/2}(\text{ns})$	ch-low	ch-high
471(3)	10	100
449(2)	20	100
440(2)	30	100
516(3)	10	70
495(3)	20	70
510(3)	30	70
471(3)	10	140
454(3)	20	140
449(3)	30	140
476(3)	9	180

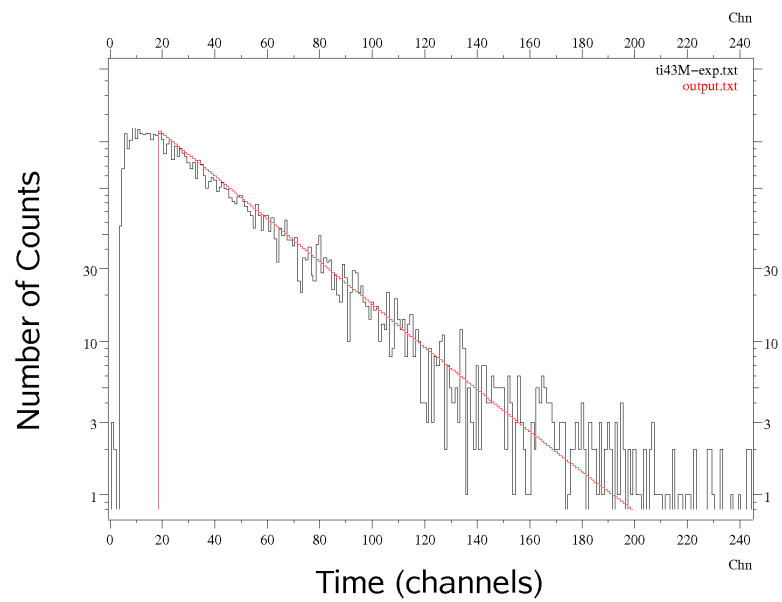


Figure 5.17: Time evolution of the addition of all the peaks in the medium range (resolution of 25ns per channel) for ^{43}Ti , along with an example adjustment. The vertical axis uses a logarithmic scale.

Table 5.6: Result of the fit on the addition of all the peaks in the medium resolution range for ^{43}Ti . It makes us conclude that the half life time for the $19/2^-$ band is of 541(4)ns, comparable to the 560(6) from the literature.

$T_{1/2}(\text{ns})$	ch-low	ch-high
540.43(4)	15	400
541.57(4)	20	400
537.33(4)	30	400
543.48(4)	10	400
538.29(4)	15	200
540.43(4)	15	300
540.43(4)	15	500
540.43(4)	15	600
543.48(4)	10	600
538.16(4)	50	600

5.5.2 ^{38}K Isomeric Analysis

As can be seen in Figure 5.9, only one band is present. Just like in the case of the $19/2^-$ band in ^{43}Ti , the other states have a lifetime that is negligible with respect to that of the 7^+ state. Therefore, an addition of the areas of all the peaks was performed. The results of this time spectrum can be found in Table 5.7.

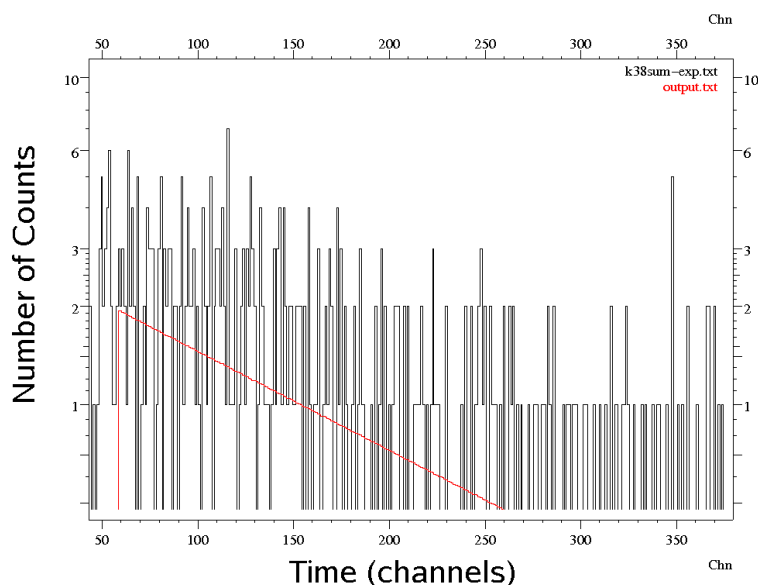


Figure 5.18: Time evolution of the addition of all the peak in the Long range (resolution of 200ns per channel) for ^{38}K , along with an example adjustment. The vertical axis uses a logarithmic scale.

What is first noticeable after seeing the result of the fit is that $T_{1/2}$ is different from the literature value. The problem with our results is that they are not so reliable as previous investigations for they have very low statistics. They have, hence, a statistical value that is not significant enough. To have closer access to the sources where this half life came from we refer to [16, 17, 18].

5.5.3 ^{45}Cr Isomeric Analysis

The results of the isomer studies of ^{45}Cr are shown in Figure 5.19 and Table 5.8. An unusual behaviour for this time spectrum is that apparently the number of counts started to augment at a certain point. The hypotheses for such a behaviour will be examined in the following chapter. Since the number of counts was so small it was decided to compress the channels by a factor of 50. This helps to visualize more clearly the trend of the plot. Because of this reemerging of the function around half

Table 5.7: Result of the fit on the addition of all the peaks in ^{38}K in the long time range. The result of this adjustment is of $18.5(13) \mu\text{s}$, according to the literature the expected value is $21.98(11)[14] \mu\text{s}$

$T_{1/2}(\text{ns})$	ch-low	ch-high
19833(85)	60	260
19016(78)	50	260
18861(77)	70	260
17243(65)	70	240
18193(72)	60	240
17504(67)	50	240
18785(77)	50	280
18861(77)	70	280
19498(83)	60	280
17637(68)	50	320

of the spectrum it was hard to judge how appropriate was a time interval. What we can conclude for the moment is that $T_{1/2} \geq 130\mu\text{s}$ (using the result from the red curve in Figure 5.19). We can affirm this because this result is for an interval that gives a relatively slanting slope. Since for a certain selection the slope can lead to results that tend to $T_{1/2} \rightarrow \infty$ then we can only say that $T_{1/2}$ is bigger than the smallest possible result (see the green curve in Figure 5.19).

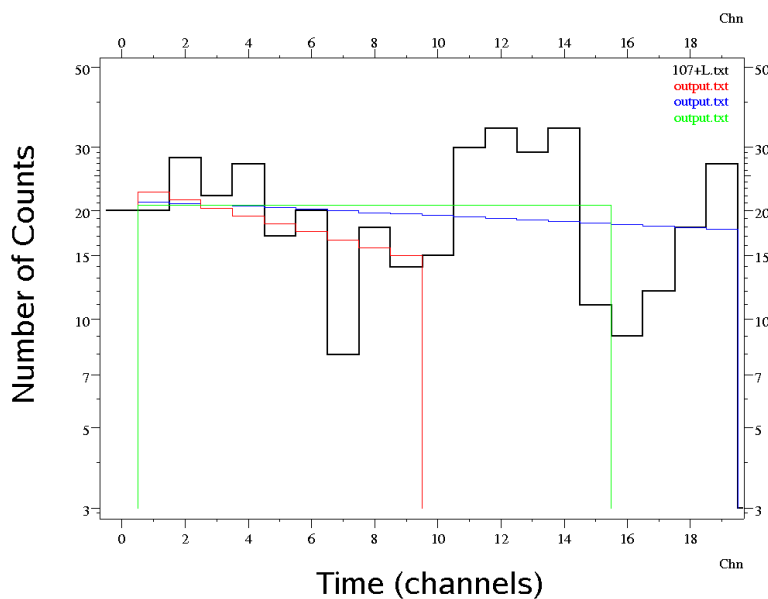


Figure 5.19: Time evolution of the 107 keV peak in the long time range for ^{45}Cr , along with three example adjustment (in red, green and blue). The vertical axis uses a logarithmic scale. Note the unexpected increasing in the number of counts after channel 10. A compression of channels by a factor of 50, i.e., the addition of counts every 50 channels into one, was performed. This corresponds to $10\mu\text{s}$ per channel.

Table 5.8: Result of the fit of 107 keV in the long time range for ^{45}Cr . There is seemingly no clear adjustment for this spectrum.

$T_{1/2}(\mu\text{s})$	ch-low	ch-high
137(1)	2	10
712(2)	2	20
$\rightarrow \infty$	2	16

Chapter 6

Analysis and Conclusions

After obtaining results for our experiment called ^{43}V , we can say we have succeeded on a whole at finding isomeric transitions in several isotopes of the nuclidic chart of elements. However, a general outlook must be done on the entire work in order to make a more complete balance of up to what extent one can be satisfied and up to which the expectations were not fulfilled. All of this is made in order to discuss further the scope and reliability of the experimental data and in order to make suggestions on how to improve similar experiments in the future.

6.1 Data Acquisition and Isotope Differentiation

We can say first that the technique of projectile fragmentation and afterwards isotope separation via the FRagment Separator proved again to be effective in order to obtain isotopes in excited states. Using a thin wedge and a thick S4 degrader allowed us to cover a big area of isotopes (24 in total) and still remain with high enough statistics.

The computer simulation made by LISE++ resulted very helpful in order to optimize the experiment conditions such as the angles, the targets, etcetera. Both LISE++ and MOCADI were also a very good aid in order to estimate if the S2 and S4 positions in the experiment were the correct ones. It is true that this position could not be corroborated in S2 because of the collocation of slits. But the positions in S4, although they were not exactly the same as in the experiment, we could see that in both cases there was a strong correlation between the positions by just allowing a compressing and shifting in the experiment with respect to the simulations.

The calibration and isotope identification of the experiment worked flawlessly. All the elements were perfectly identified with distributions narrow enough as to make difference between two of them easily. The FRagment Separator in combination with all its detectors proved to be the ideal for correct in-flight identification of the isotopes. This in-flight identification was fundamental to obtain the energy vs time matrices for all the isotopes.

One of the main inconveniences of this experiment was the problem of the gas chambers in the MW detectors. In any case this was only a casual error and not a systematic one. One can see however that the development of the two tracks helped us obtaining better statistics, especially for the lightest elements. Let us not forget that one of the isotopes that had isomeric states was ^{38}K . Without the development of Track1 scheme it would have been virtually impossible to obtain acceptable statistics for this isotope. It would have been indeed better to have calibrated pressure in the gas chambers of the MW's and this way not having to approximate the trajectories of the isotopes in the FRS. But once the experiment has been done and it has collected valuable data what is left to do is try to make the best of the results. And this development of tracks did represent an excellent choice to solve the problems of low statistics because of a casual error in the performance of the experiment.

6.2 Isomeric Analysis

After doing a correct in-flight identification of the isotopes, gating on each isotope was possible in order to obtain an energy vs time matrix. With this matrix it was not only possible to have a complete picture of how the decay happened after the prompt flash, but it also was quite convenient in order to make projections of time and energy for obtaining time or energy spectra. Having scanned several isotopes was useful to recognize the background lines (that were indeed present in all isotope matrices). Having abundant isotopes like ^{42}Ti and ^{44}V with no isomeric transitions in this experiment was useful to clean our spectra from the background and even from the $^{\text{nat}}\text{Ge}(n,n'\gamma)$ in the case of the medium range isomeric lines in ^{43}Ti . The method of simply subtracting the background from a later time and the same length was equally good for the background lines but not to cancel out the $^{\text{nat}}\text{Ge}(n,n'\gamma)$.

We were capable of isolating all the energies from isomeric transitions in a E_γ spectrum. With this the exact position of the peaks could be determined and the channels that worked as background could be determined more easily. The gate in the energy axis led to time matrices that were satisfactory in all the shown cases. We now focus individually on the results from every isotope we studied:

6.2.1 ^{43}Ti

In Figures 6.1 to 6.3 we show according to the shell model how the states of the nucleons in ^{43}Ti would look like in order to understand the transitions. We will omit the $1s_{1/2}$, $1p_{3/2}$, $1p_{1/2}$, $1d_{5/2}$ and $s_{1/2}$ shells from the drawings since they will always be filled. In total we will have 16 neutrons and 16 protons in such shells. In Figure 6.1 we show the configuration of the ground state. It is clearly the ground state because all nucleons are in their lowest state. The state is named after the only uncoupled nucleon, i.e., the single neutron in the $f_{7/2}$ shell. In Figure 6.2 the excitation of the first state is shown. In here one of the neutrons from the $d_{3/2}$ goes to the shell just above it. The empty position is the one that gives the label to the state since the neutron in the $f_{7/2}$ shell is now coupled. In Figure 6.3 a simplified version of the other isomeric state is shown. In this $19/2^-$ state one of the protons changes its

projection with respect to the other. However, even if they are parallel, they can clearly not have the exact same spin projection because of the Pauli principle. In the highest possible energy state one of the protons has $m = 7/2$, while the other one has $m = 5/2$. The addition of all the m 's that are uncoupled leads to $7/2 + 7/2 + 5/2 = 19/2$, which corresponds to the $19/2^-$ state. In the other intermediate configurations, $15/2^-$, $11/2^-$, several combinations of spin projections can happen so that the addition gives such results.

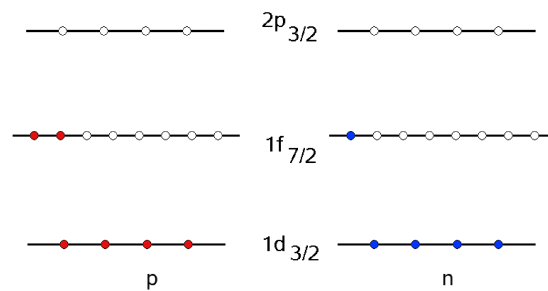


Figure 6.1: Ground state configuration ($7/2^-$) according to the shell model for ^{43}Ti .

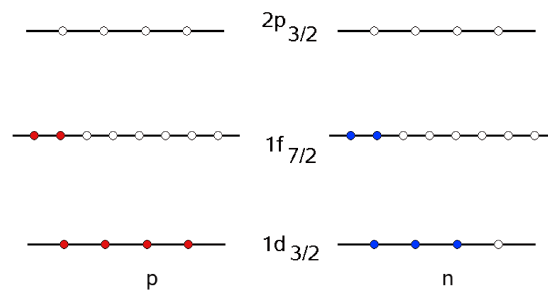


Figure 6.2: First excited state configuration ($3/2^+$) according to the shell model for ^{43}Ti .

Two different isomeric states were found for ^{43}Ti . The first one, the $3/2^+$ isomer transition to the ground state was perfectly identified with overwhelming statistics. It was tried to calculate the same $T_{1/2}$ in the medium time range and a not discardable result was obtained. Our final result for this 313 keV peak did not have a common range with the literature value. In this case it is worth considering this result as valid for it was obtained with enough statistics in order to revise the commonly accepted values.

For the other structure, i.e., the decay from the $19/2^-$ isomer to the ground state, passing through all the intermediate states, the different peaks lead to different $T_{1/2}$,

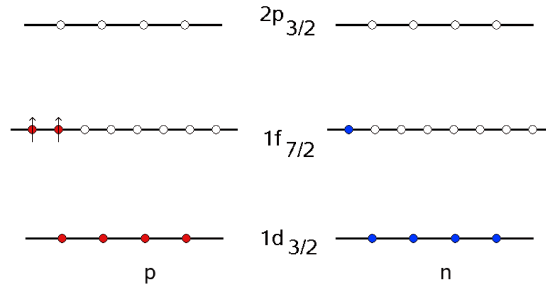


Figure 6.3: Second band configuration ($19/2^-$ to $11/2^-$) according to the shell model for ^{43}Ti .

it could be argued that the half life of the intermediate states are very small compared to that of the $19/2^-$ state. For this reason adding the counts from all three of the transitions did make sense, affirming that the analogy to the mirror nucleus ^{43}Sc is right. The only inconvenience of this is that the lifetimes of these transitions are not very similar to each other. But in any case we can affirm that the obtained result of adding the counts from the three of them leads to a result that is close to the one expected. An alternative for this method could have been to do a weighted average of them, just like for the 312 keV peak. The result of such a method is 513(5). The only problem of this alternative method is that considering the error as the weight gives too much importance to the result that has the smallest uncertainty, that is based only on statistical parameters. We know, for instance, that the 115 peak was one of the least reliable ones, not only for the statistics but because it was the one with the biggest background. Therefore, using the addition of all the peaks is definitely the best way to consider all statistics with their corresponding relevance. In Table 6.1 we show a summary of all the transitions seen in ^{43}Ti .

Table 6.1: Summary of all the transitions seen in ^{43}Ti and their characteristics according to the shell model.

E_γ (keV)	initial state	final state	σL
313	$3/2^+$	$7/2^-$	M2
115	$19/2^-$	$15/2^-$	E2
1094	$15/2^-$	$11/2^-$	E2
1858	$11/2^-$	$7/2^-$	E2

6.2.2 ^{38}K

The ground state of ^{38}K is shown in Figure 6.4. In this one the addition of the decoupled neutron and proton leads to the 3^+ ground state. In Figure 6.5 both the decoupled proton and neutron jump up to the $f_{7/2}$ shell, projections m are parallel and equal to $7/2$. For the intermediate state 4^- , shown in Figure 6.6, only one nucleon from the $d_{3/2}$ shell goes to $f_{7/2}$. This leaves us with the possibility to find isomeric states with spins from 2^- to 5^- . The 6^- configuration, pictured in Figure 6.7, can happen in a configuration like in 4^- but with the difference that one of the two nucleons just below the excited one change its spin projection m . This way we are able to produce states from 0^- to 7^- . Note that in the schemes for these two the nucleons are painted all with the same colour since this could be either neutron or proton excitation.

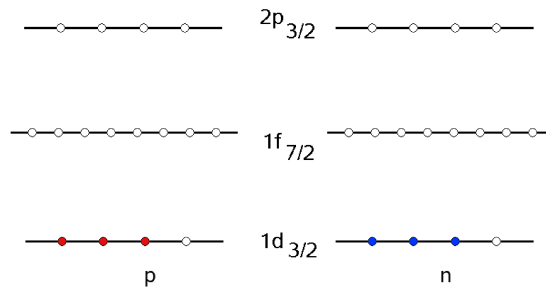


Figure 6.4: Ground state configuration (3^+) according to the shell model for ^{38}K .

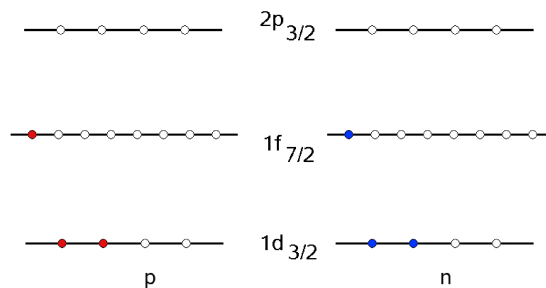


Figure 6.5: 7^+ configuration according to the shell model for ^{38}K .

For ^{38}K all the isomers from the only band of interest for the present work were in the long range. Since individually they all had such low statistics it had no sense to make a fit for every peak. It was decided to add them all. The addition offers fairly enough statistics as to make respectable result for $T_{1/2}$. In future experiments it could be interesting to perform an experiment similar to this one but in which the covered isotopes were narrowed to very few and focused exclusively on ^{38}K , like

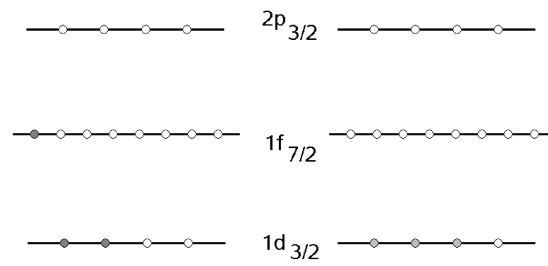


Figure 6.6: 4^- configuration according to the shell model for ^{38}K .

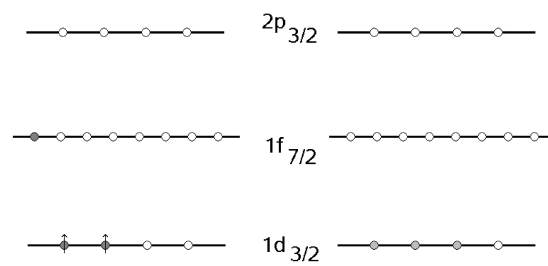


Figure 6.7: 6^- configuration according to the shell model for ^{38}K .

in other experiments from the RISING campaign. With such an approach we could obtain results as to compare the fit for every peak and do an estimation of the half life times for all the intermediate states. Another thing is that the result was not too close to the literature value. This result once again cannot be considered as being an influential measure since the statistics of it left a lot to be desired.

Table 6.2: Summary of all the transitions seen in ^{38}K and their characteristics according to the shell model.

E_γ (keV)	initial state	final state	σL
38 (not seen)	7^+	6^-	(E1)
812	7^+	4^-	E3
774	6^-	4^-	E2
2646	4^-	3^+	E1
3420	6^-	3^+	E3

6.2.3 ^{45}Cr

As was mentioned already, the decay scheme of ^{45}Cr was not known. However, by using its mirror nucleus, ^{45}Sc , we can say that the 107 keV transition most likely corresponds to either a transition from $3/2^+$ or $3/2^-$ to the ground state (see Figure 6.8), $7/2^-$. The $3/2^+ \rightarrow 7/2^-$ (see Figure 6.9 is essentially the same as in ^{43}Ti . The $3/2^- \rightarrow 7/2^-$ transition (see Figure 6.10) happens when the uncoupled proton in $f_{7/2}$ goes one step up to the $p_{3/2}$ shell.

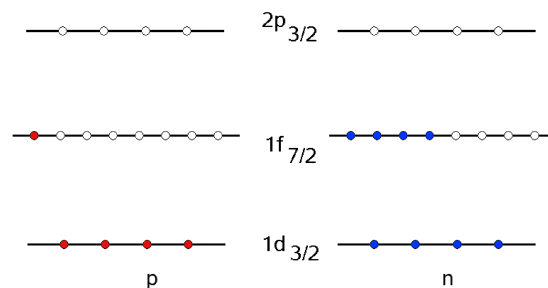


Figure 6.8: Ground state configuration ($7/2^-$) according to the shell model for ^{45}Cr .

For this element we repeat the recommendation of making a projectile fragmentation experiment to focus only on this isotope. With it we could have obtained a much better decay scheme for ^{45}Cr . This lack of statistics made it very hard to obtain

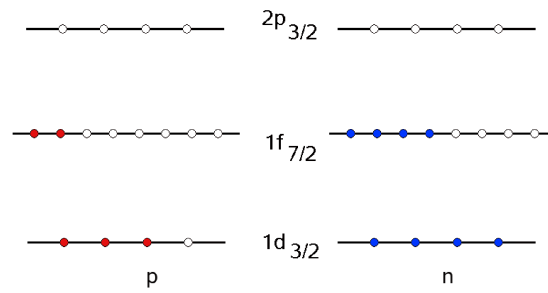


Figure 6.9: The most probable first excited state configuration ($3/2^+$) according to the shell model for ^{45}Cr .

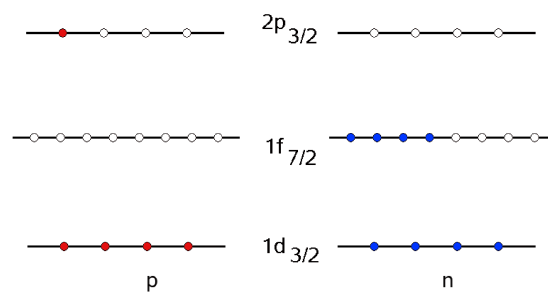


Figure 6.10: The second most probable first excited state configuration ($3/2^-$) according to the shell model for ^{45}Cr .

a good estimate of the half life. One possible explanation for this behaviour is the presence of other transitions from levels higher than $3/2^-$ had very similar lifetimes. But in any case, obtaining an estimate of the $T_{1/2}$ for this first time seen isomer is an irrefutable advance in the quest for probing the nature of isomeric states in isotopes of the nuclidic chart of elements.

Table 6.3: Summary of the two possibilities for the 107 keV transition seen in ^{45}Cr and its characteristics according to the shell model.

E_γ (keV)	initial state	final state	σL
107	$3/2^+$	$7/2^-$	M2
107	$3/2^-$	$7/2^-$	E2

Chapter 7

Popularvetenskaplig Sammanfattning

Isomeriska studier i $f_{7/2}$ -skalet

Kärnfysiken har spelat en viktig roll i den moderna vetenskapen under ca hundra år. Vi jobbar med att förbättra våra modeller för hur atomkärnor beter sig under olika omständigheter. Experimentet som detta examensarbete handlar om är ännu en viktig pusselbit i förståelsen av samspelet mellan protoner och neutroner. Vi försöker analysera relativt långlivade isomeriska övergångar i isotoper i närheten av ^{43}V i nuklidkartan. Ett isomeriskt tillstånd är ett kärntillstånd som har högre energi än i sitt grundtillstånd. Vårt slutgiltiga mål är att bestämma livstiden hos alla isomerer som vi kan hitta.

I arbetet beskriver jag den experimentella metod som används för studiet av kärnorna. Vi använde en teknik som heter ”projectile fragmentation”, eller projektilfragmentation. Vi hittade 24 kärnsorter, men bara tre av dem hade synbara isomeriska tillstånd. Fastän vi upptäckte många intressanta egenskaper är det nog isomerernas halveringstider som är viktigast.

Som medel till att förutsäga vilka kärnor sannolikt har isomeriska tillstånd använde vi teorin med spegelkärnor. Enlig våra teoretiska modeller är den förhållandevis bindningen inne i en kärna den starka kraften som är densamma för båda neutroner och protoner, vilka kan bli betraktas som olika tillstånd av samma partikel. Tvåkärnor kallas ”spegel kärnor” om de har den samma massa och antalet protoner respektive neutroner är utbytt mot varandra. Med kunskap om de isomeriska tillstånden i en kärna kan vi vänta oss samma mönster i den spegelkärna vi undersöker. Vi använder alltså redan känd kunskap för att finna ny.

En tidigare okänd isomer, ^{45}Cr , har upptäckts. Vi kunde tyvärr inte bestämma dess halveringstid för vi producerade inte isotopen i tillräckligt stor mängd. Vi kunde bara göra en vag uppskattning av halveringstiden. För att öka våra kun-

skaper om kärnstruktur måste vi fortsätta detta arbete. Men vi kan nu säga att vi är på rätt spår.

Chapter 8

Acknowledgments

The list of persons I would thank for the accomplishment of this project is a never ending one. Although the first person to thank is, of course, my supervisor, Dirk Rudolph. Without his help, patience and understanding during all these long months of hard work this project could have never been accomplished. I thank professor Rudolph for providing me with the priceless fortune of initiating myself in the discipline of Nuclear Physics. Professor Rudolph was also responsible for the calibration of the experiment and for developing the software to analyze all the data of the experiment.

At the same time I would like to thank my so-called “semi-supervisor” Robert Hoischen. His work was my most important reference for the making of this Master Thesis. Robert was entirely responsible for the computer simulations in both LISE++ and MOCADI.

I also have to thank enormously the invaluable help given by Lise-Lotte Andersson, Emma Johansson, and Diego Torres in the realization of this work. Without their advice in every single aspect of the achievement the accomplishment of my project would have been much more difficult and tedious.

Special thanks to the entire Division of Nuclear Physics. I will never forget all the overwhelming kindness I was received with. All the personnel made me feel at home.

I would also like to thank all the “kompisar” I made while here in Lund, Sweden. The same way I want to thank Lund University and Universidad Simón Bolívar for the wonderful opportunity we, students from both Academic Institutions, are given to do such an enriching and fulfilling experience as is this bilateral exchange program. I hope such initiatives can not only continue existing, but improve so that every year more and more students have the chance to study for some time abroad in order to interact with other cultures. This has been a year I shall never forget.

I could not finish these lines without thanking last, but not the least, my family and friends from my home country, Venezuela. Especially thanks to my Parents, Ana and Fernando, who are responsible for my upbringing, making me feel like the

most thankful and proud son one could think of. Thanks for all the support given to me throughout my life and for becoming my role models. Thanks to my sister, Eva, for being my companion from the day I was born. Thanks to the rest of my family for being always there for me. You are the real people this work is dedicated to.

May happiness be always with all of you.

Bibliography

- [1] R. Pfaff, Ph.D. Thesis, Michigan State University (1996).
- [2] R. Serber, Phys. Rev. 72, 1114 (1947).
- [3] K.S. Krane, “Introductory Nuclear Physics”, John Wiley & sons, New York (1988).
- [4] K.L.G. Heyde, “The Nuclear Shell Model”, Springer Verlag, Heidelberg (1994).
- [5] Jörgen Ekman, Ph.D. Thesis, Lund University (2004).
- [6] H. Morinaga and T. Yamazaki, “In-Beam Gamma-Ray Spectroscopy” North-Holland Publishing Company, Amsterdam, New York, Oxford (1976).
- [7] K. Heyde, “Basic Ideas and Concepts in Nuclear Physics”, Institute of Physics Publishing, Bristol (1994).
- [8] A. Bohr and B.R. Mottelson, “Nuclear Structure Vol. 2”, Benjamin Inc., New York (1975).
- [9] Schmidt-Ott et al., Z.Phys. A 350, 215 (1994).
- [10] R. Hoischen, *An Isomer Study of the Nucleus ^{54}Ni ; Preparations, Simulations, and First Results*, March 2006.
- [11] H. Bichsel, D.E. Gordon and S.R. Klein, *PASSAGE OF PARTICLES THROUGH MATTER*, April 2006.
- [12] Pascale Mayet, P. D. Thesis, GSI Darmstad, 2000.
- [13] Margareta Hellström and Marek Pfützner, *The FRS Data Acquisition Manual*, December 1997.
- [14] *Evaluated and Compiled Nuclear Structure Data: ENSDF and XUNDL Dataset Retrieval*: <http://www.nndc.bnl.gov/ensdf/>
- [15] Chemoff H., Lehmann E.L., *The use of maximum likelihood estimates in χ^2 tests for goodness-of-fit. The annals of Mathematical Statistics*, 1954.
- [16] *Data from AR38K-38019007.ens*: <http://www.nndc.bnl.gov/useroutput/AR038K-38019007.html>

- [17] *Data from AR38K-38019003.ens*: <http://www.nndc.bnl.gov/useroutput/AR038K-38019003.html>
- [18] *Data from AR38K-38019005.ens*: <http://www.nndc.bnl.gov/useroutput/AR038K-38019005.html>